

University of Alberta

Heat Transfer Analysis of Flame-sprayed Metal-polymer Composite Structures

by

David Stuart Therrien

A thesis submitted to the Faculty of Graduate Studies and Research
in partial fulfillment of the requirements for the degree of

Master of Science

Department of Mechanical Engineering

©David Therrien

Spring 2013

Edmonton, Alberta

Permission is hereby granted to the University of Alberta Libraries to reproduce single copies of this thesis and to lend or sell such copies for private, scholarly or scientific research purposes only. Where the thesis is converted to, or otherwise made available in digital form, the University of Alberta will advise potential users of the thesis of these terms.

The author reserves all other publication and other rights in association with the copyright in the thesis and, except as herein before provided, neither the thesis nor any substantial portion thereof may be printed or otherwise reproduced in any material form whatsoever without the author's prior written permission.

Abstract

The temperature distribution of a flame-sprayed metallic layer on glass fiber-reinforced epoxy flat plates was determined experimentally, analytically, and numerically. The composite samples consisted of flat composite glass fiber-epoxy plates fabricated by filament winding, a layer of garnet sand embedded in the epoxy, with similar thermal properties to the glass fiber-epoxy layer, and a flame-sprayed aluminum-silicon (Al-12Si) coating. The use of garnet sand to promote adhesion of the metallic coating during flame spraying is novel. A second set of samples had a top layer of glass fiber wound above the coating. A resistive heating wire was attached to the coated surface at the leading edge of both sets of samples, while the polymer and coating surfaces were exposed to forced convective cooling in a wind tunnel. Thermocouples were attached to the polymer and coating to measure the transient and spatial surface temperature distributions. Both the coating and polymer surfaces experienced significant temperature increases near the heating source, with a uniform decay of the surface temperature away from the source. The surface temperature of the coating was appreciably higher than that of the polymers, away from the heating source. The use of a metallic coating to conduct heat on polymer structures is also novel, and the results indicate that the metallic coating is an effective conductor, while the polymer acts as an insulator.

Acknowledgements

Firstly, I would like to express my sincere gratitude to my supervisor, Dr. Andre McDonald and co-supervisor, Dr. Pierre Mertiny. Without their support in graduate studies this would not have been possible. The trustful relationship that I experienced with both made my graduate studies a productive and enjoyable experience. They taught me both engineering principles, but also professionalism while enjoying work. Their guidance, spoken and unspoken, allowed me to learn from their experience.

I have learnt very practical lessons along this journey. I would like to acknowledge the discussions and help with Bernie Faulkner and Rick Conrad. I appreciate having being able to use experiments to contribute to my graduate experience, and without their assistance it would not have been possible.

I have greatly enjoyed discussions with other students during my studies. From discussing very technical topics walking to the bus, to debating political ideologies while there was thesis work to complete, I would like to acknowledge Natanael Melendez, Navid Pourjavad, Mark Roes, Shishir Rao, Daniel Booy, and Farzan Tavakoli among many others. I would further like to acknowledge my lab mates other the last two years, in our 6-25 lab space were we all sweated together during the summer, and lacked sunlight in the winter. The different backgrounds and cultural experiences of all the people encountered added greatly to my life experience.

I would like to acknowledge the assistance of my friends during this graduate experience. Sometimes just sharing a lunch or laugh made my day. Whether you realized it or not, your listening helped me focus on what was important. I would like to acknowledge: Adam Burke and Stephanie Ridge, may we continue to hike and discuss log cabins together; Nicole and Justin Kingston, for both of you your cooking and wisdom are amazing; Paul Kirwan and Sean Pellatt, your perspectives made running and everything else enjoyable; Bobby Williamson and Julien Fitamant, everything from discussions with milk and cookies, to swim training, thank you for the friendship. Thank you to my girlfriend Jessica Stowe for her support and patience. Finally, I would like to thank my family for their support throughout the last two years. Their support, from Sunday dinners to enabling discussion with Boeing engineers has been appreciated.

Table of Contents

Chapter 1 Introduction	1
1.1 Background.....	1
1.1.1 Heat Transfer.....	2
1.1.2 Thermal Spraying.....	5
1.1.3 Polymers.....	9
1.2 Previous Studies.....	10
1.3 Objectives.....	14
1.4 Thesis organization	15
1.5 References.....	16
Chapter 2 Experimental Method	22
2.1 Polymer Fabrication	22
2.2 Flame Spraying	25
2.3 Coating Characterization	27
2.4 Heating and Temperature Measurement	28
2.5 Numerical Method.....	34
2.6 References.....	36
Chapter 3 Results and Discussion.....	37
3.1 Coating Characterization	37
3.2 Investigation of Fiber Damage.....	44

3.3	Experimental Results.....	48
3.3.1	Insulated Tests	48
3.3.2	Wind Tunnel – Test #1 with Coating Exposed.....	60
3.3.3	Wind Tunnel – Test #2 with Top Polymer Layer	70
3.4	Analytical Model.....	77
3.4.1	Governing Equation and Assumptions.....	77
3.4.2	Heat Transfer Coefficient	81
3.4.3	Curve Fitting.....	85
3.4.4	Temperature Distribution	91
3.5	Numerical Model	95
3.5.2	Wind Tunnel – Test #1 with coating exposed	97
3.5.3	Wind Tunnel – Test #2 with top polymer layer	102
3.6	References.....	106
Chapter 4 Conclusions		111
4.1	Future Work	113
4.2	References.....	115
Appendix		116
4.3	Appendix 1.....	116
4.3.1	MATLAB Code:	116

List of Tables

Table 2.1: Number of layers of fibers and passes during flame spraying.....	27
Table 2.2: Summary of geometry for numerical analysis	35
Table 3.1: Thickness and volume fractions of the layers	39
Table 3.2: Thermal conductivities of the layers	53
Table 3.3: Summary of experimental parameters.....	76
Table 3.4: Air properties	81
Table 3.5: Model parameters	96

List of Figures

Figure 1.1: Schematic of flame spraying [20]	6
Figure 1.2: Gas temperatures and velocities for various thermal spray processes [21, 22].....	7
Figure 2.1: Image of the tensioning system and resin bath.....	24
Figure 2.2: Image of polymer fabrication	24
Figure 2.3: Image of flame spraying polymer substrate	26
Figure 2.4: Schematic of the electrical circuit.....	29
Figure 2.5: Image of the electrical components.....	29
Figure 2.6: Image of coated polymer plate for insulated tests.....	31
Figure 2.7: Image of embedded metallic coating for wind tunnel tests	33
Figure 2.8: Image of the control experiment	34
Figure 3.1: Image of coated polymer plate	38
Figure 3.2: SEM image of coating on garnet sand-polymer composite substrate.....	40
Figure 3.3: SEM image of un-molten and semi-molten coating particles.....	40
Figure 3.4: Magnification (250x) of a) coating on garnet sand-polymer composite substrate and with EDS mapping for b) Calcium (Ca), c) Silicon (Si), d) Oxygen (O), e) Aluminum (Al) and f) Iron (Fe).....	42
Figure 3.5: XRD pattern of the coating	43
Figure 3.6: Cross-sectional view of fire-damaged GFRP [7]	46
Figure 3.7: Temperature measurements along front garnet sand and rear polymer surfaces during flame spraying	47

Figure 3.8: Transient temperature profile of coating surface.....	49
Figure 3.9: Transient temperature profile of polymer surface	49
Figure 3.10: Transient temperature profile of garnet sand surface – Control	50
Figure 3.11: Transient temperature profile of polymer surface – Control	50
Figure 3.12: Spatial temperature profiles of the coating and uncoated garnet sand (control) surfaces after 5 minutes of heating (insulated tests)	57
Figure 3.13: Spatial temperature profiles of the rear polymer (coating and control) surfaces after 5 minutes of heating (insulated tests)	57
Figure 3.14: Spatial temperature profiles of the coating and uncoated garnet sand (control) surfaces after 10 minutes of heating (insulated tests)	58
Figure 3.15: Spatial temperature profiles of the rear polymer (coating and control) surfaces after 10 minutes of heating (insulated tests)	58
Figure 3.16: Spatial temperature profiles of the coating and uncoated garnet sand (control) surfaces after 30 minutes of heating (insulated tests)	59
Figure 3.17: Spatial temperature profiles of the rear polymer (coating and control) surfaces after 30 minutes of heating (insulated tests)	59
Figure 3.18: Transient temperature profile of coating surface for air flow at 27.8 m/s	62
Figure 3.19: Transient temperature profile of polymer surface for air flow at 27.8 m/s	62
Figure 3.20: Transient temperature profile of garnet sand for airflow at 27.6 m/s (at heating wire) – Control.....	64
Figure 3.21: Transient temperature profile of garnet sand for airflow at 27.6 m/s (away from heating wire) – Control.....	65

Figure 3.22: Transient temperature profile of polymer surface for airflow at 27.6 m/s – Control	65
Figure 3.23: Transient temperature difference between the coating and garnet sand (control) surfaces ($T_C - T_{\text{Sand}}$)	67
Figure 3.24: Transient temperature difference of the rear polymer (coating and control) surfaces ($T_C - T_{\text{Sand}}$)	67
Figure 3.25: Spatial temperature profile of the coating and polymer surfaces after 6 minutes of heating.....	68
Figure 3.26: Transient temperature profile of the coating (layer thickness = 0.51 mm).....	71
Figure 3.27: Transient temperature profile of the top polymer surface (layer thickness = 0.9 mm)	71
Figure 3.28: Transient temperature profile of the bottom polymer surface (layer thickness = 9.2 mm).....	72
Figure 3.29: Spatial temperature profiles of coating, top and bottom polymer surfaces.....	75
Figure 3.30: Overview of samples.....	79
Figure 3.31: Boundary conditions of polymer samples	80
Figure 3.32: Spatial temperature profile of coating surface with expected trend line – 1 st wind tunnel test with coating exposed	87
Figure 3.33: Spatial temperature profile of coating with alternative trend line – 1 st wind tunnel test with coating exposed	88
Figure 3.34: Spatial temperature profile of coating surface with expected trend line – 2 nd wind tunnel test with top polymer layer.....	89

Figure 3.35: Spatial temperature profile of coating with alternative trend line – 2 nd wind tunnel test with top polymer layer.....	90
Figure 3.36: Experimental and analytical results of polymer surface – 1 st wind tunnel test with coating exposed	92
Figure 3.37: Experimental and analytical results of top and bottom polymer surfaces – 2 nd wind tunnel test with top polymer layer	93
Figure 3.38: Mesh applied to geometry of second wind tunnel experiment ...	96
Figure 3.39: Numerical temperature results – 1 st wind tunnel test with coating exposed	97
Figure 3.40: Experimental and Numerical Results – 1 st wind tunnel test with coating exposed	98
Figure 3.41: Numerical transient results – 1 st wind tunnel test with coating exposed.....	102
Figure 3.42: Numerical temperature results – 2 nd wind tunnel test with top polymer layer	103
Figure 3.43: Numerical surface temperatures – 2 nd wind tunnel test with top polymer layer	103

Nomenclature and Abbreviations

1.1.1 List of Symbols:

A, B, C, D	Constants
Bi	Biot number, $Bi = hL_c/k$
c	Speed of sound (m/s)
C_p	Specific heat capacity (J/kg-°C)
Fo	Fourier number, $Fo = at/L_c^2$
h	Heat transfer coefficient (W/m ² -°C)
k	Thermal conductivity (W/m-°C)
L	Length (m)
Ma	Mach number, ($Ma = U/c$)
Nu	Nusselt number, ($Nu = hL_c/k_f$)
Pr	Prandtl number, ($Pr = \nu/\mu$)
q'''	Volumetric energy generation (W/m ³)
r	Recovery factor
R	Gas constant, (air, 0.287 kJ/kg-K)
R^2	Coefficient of determination, $R^2 = 1 - \frac{SS_{\text{err}}}{SS_{\text{tot}}}$
Re	Reynolds number, ($Re = \rho UL_c/\mu$)
SS_{err}	Residual sum of squares, $SS_{\text{err}} = \sum_e (T_e - T_i)^2$
SS_{tot}	Total sum of squares, $SS_{\text{tot}} = \sum_e (T_e - \bar{T}_e)^2$
ν	Volume fraction

U	Velocity (m/s)
t	Time (s)
T	Temperature (°C, K)
x, y, z	Linear coordinates (m)

1.1.2 Greek Symbols

α	Thermal diffusivity (m^2s^{-1})
ε	Error
γ	Specific heat capacity ratio
μ	Dynamic viscosity (Pa·s)
ρ	Density (kg/m^3)

1.1.3 Subscripts

0	At the wall surface
∞	Free stream
air	Air
Al	Aluminum
Analyt.	Analytically calculated
aw	Adiabatic wall
c	Characteristic
C	Coating
e	Experimentally measured

f	Fluid
fm	Film
i	Surface, curve fit
L	Length
Metal	Metallic coating
P	Polymer
Sand	Garnet sand surface
Si	Silicon
tr	Transitional
x	X-coordinate

1.1.4 Superscripts

^	Substitution
-	Average value
*	Non-dimensional variable

1.1.5 List of Abbreviations

Al-12 Si	88 wt. % aluminum, 12 wt. % silicon
EDX	Energy Dispersive Spectroscopy
DC	Direct Current
FEA	Finite Element Analysis
FMR	Flow Meter Reading

FRP	Fiber Reinforced Polymers
HVOF	High Velocity Oxy-Fuel
MDA	Malondialdehyde ($\text{CH}_2(\text{CHO})_2$)
NLPM	Normal Liters Per Minute
PEEK	Polyether Ether Ketone
PFA	Paraformaldehyde
PMC	Polymer Matrix Composite
PTFE	Polytetrafluoroethylene
SEM	Scanning Electron Microscopy
XRD	X-Ray Diffraction

Chapter 1 Introduction

1.1 Background

The adverse effects of ice formation along airfoils have been a crucial design problem since the beginning of commercial air travel. The drag coefficient can increase by over 30% due to icing on an airfoil [1]. During take-off, when aircrafts have decreased stall margins, these effects can be particularly hazardous. Traditional in-flight de-icing methods include blowing hot engine “bleed” air along the thin metal airfoil surface, which have a hollow leading edge [2]. However, the bleed air de-icing system accounts for up to 3% of the fuel consumption on modern commercial airliners [3].

As aircrafts become more efficient, more advanced materials are being used to increase fuel efficiency. Both Boeing and Airbus’ new commercial aircrafts use polymer structures due to the significant weight savings and thus fuel savings [4]. Also, as these new advanced materials are being used, traditional de-icing methods, such as using bleed air at roughly 200°C can denature the polymer airfoils [2, 5].

Due to these challenges new de-icing systems for polymer structures have been developed. The composite Boeing 787 uses an electro-thermo ice protection system, which has heating blankets incorporated into the leading edges of the airfoils. The heating blankets can be energized simultaneously or sequentially for reduced power consumption [3]. These heating blankets are

integrated into the composite airfoils, composed of carbon fibers and glass fibers above and below a spray-on metallic coating [6].

Other applications of polymers used in structural systems exposed to high speed air flows include helicopter rotor blades and wind turbines. In both of these applications, either a de-icing or anti-icing system is also necessary [7, 8]. However, most of the ice protection systems for these applications are transferred from the aerospace industry and scaled to apply to the appropriate sector [9, 10]. Polymer composites may also be used in the oil and gas industry as pipes with high strength and corrosion resistance. In order to avoid freezing in the pipes, a heating strategy will be required that may be based on heat tracing. This will ensure that the oil not only does not freeze, but also does not fall below its pour point (point below which oil does not flow), which has the adverse effects of increasing oil viscosity and pump power requirements.

1.1.1 Heat Transfer

To maintain a general application, the focus will be high speed airflows for the aerospace sector since the ice protection system technology normally originates there [9]. Initially, high speed supersonic flight was limited by the transient nature of heat transfer in the metallic airfoils [11]. These supersonic speeds are greater than the speed of sound in air (Mach 1), and due to such great speeds compressible flow effects must be accounted for. At these speeds, the temperature distribution within the metallic airfoils has been experimentally determined [12]. However, as the mechanics and fluid properties have been better understood it is possible to determine the heat

transfer more accurately and for composite airfoils [11, 13]. The heat transfer is dominated by heat conduction within the airfoil and heat convection with the air.

Heat Conduction

Heat conduction is the transfer of energy due to molecular activity [14]. This is due to a temperature difference, which by the first law of thermodynamics requires that the energy is continuously transported in the direction of decreasing temperature. The heat conduction is governed by the conservation of energy. For a stationary body with constant thermal properties this results in a general Cartesian three-dimensional transient form as shown in Eq. 1.1 [14]:

$$\frac{\partial^2 T}{\partial x^2} + \frac{\partial^2 T}{\partial y^2} + \frac{\partial^2 T}{\partial z^2} = \frac{\rho C_p}{k} \left(\frac{\partial T}{\partial t} \right) \quad (1.1)$$

The material properties that influence heat conduction include the thermal conductivity (k) and diffusivity (α). A non-dimensional number which characterizes the ratio of internal to external heat conduction resistance is called the Biot number. If the Biot number,

$$\text{Bi} = \frac{hL_c}{k}, \quad (1.2)$$

which is defined as the product of the heat transfer coefficient, h , and characteristic length of the body, L_c , divided by the material thermal conductivity, k , is much less than 1, the temperature distribution across the characteristic length will be uniform [14].

Heat Convection

Convective heat transfer is the transfer of energy “from a surface to a fluid flowing over it as a result of a difference between the temperatures of the surface and the fluid” [15]. Since the buoyancy forces are negligible relative to the forced flow, due to the relative motion between the airfoil and air flowing over it, and the fluid flow is over the outer surface of the body, the heat convection can further be defined as external forced heat convection. To further characterize the heat convection we must characterize the flow regime. The Reynolds number characterizes the flow regime, and has been identified as the ratio of inertial to viscous forces. For flow over flat plates, the transition from laminar to turbulent is “neither sudden or precise” [16]. The transition occurs at the critical Reynolds number which typically lies between 3×10^5 and 6×10^5 [16]. Another important dimensionless parameter in heat convection is the Prandtl number, which is the ratio of kinematic viscosity to thermal diffusivity. For air, the $Pr \approx 1$, and both the velocity and thermal boundary layers are approximately the same thickness [16].

The non-dimensional form of the heat transfer coefficient is the Nusselt number. The Nusselt number is defined as the product of the heat transfer coefficient and characteristic length divided by the thermal conductivity of the fluid.

$$Nu = \frac{hL_c}{k_f} \quad (1.3)$$

It represents the ratio of heat transferred from a surface to the heat conducted away by the fluid [16]. Correlations of Nusselt numbers, as a

function of the Reynolds number and Prandtl number, are well known for both laminar and turbulent flows across flat plates [17, 18].

The recovery factor, r , compensates for the fluid viscous shear work in the fluid by making use of the adiabatic-wall temperature, T_{aw} , which will be greater than the free stream temperature of the fluid [19]. For laminar flows, experimental and theoretical analyses have shown that the recovery factor can be approximated over a large range of Prandtl numbers, velocities, and geometrical shapes [12] as the square root of the Prandtl number. For turbulent flows, experimental analyses have shown that the recovery factor is approximately the cubic root of the Prandtl number [19]. Note that the Prandtl number is near unity for air, and as such, the laminar and turbulent recovery factors are also near unity.

1.1.2 Thermal Spraying

Thermal spraying is a group of processes that are used to fabricate hard-faced coatings. The principle behind thermal spraying, where a spray material is fed through a spray gun and onto the prepared surface of the substrate, is shown in Fig. 1.1 for flame spraying [20]. The spray materials are micron-sized particles which are accelerated towards the substrate through the spray gun. Regardless of the process, the particles and substrates can be fabricated from metals, metal alloys, ceramics or polymers [21]. Several common processes include cold spraying, wire arc, air-plasma spraying, flame spraying and high velocity oxy-fuel (HVOF) each with a

unique combination of heat source and particle velocity. The ranges of temperatures and velocities are summarized in Fig. 1.2 [21, 22].

Thermal-sprayed coatings are used in a variety of applications because they offer improved wear resistance, heat resistance (thermal barrier coatings), dimensional control, oxidation resistance, corrosion resistance, dimensional restoration, and electrical properties (conductivity and resistivity) [21].

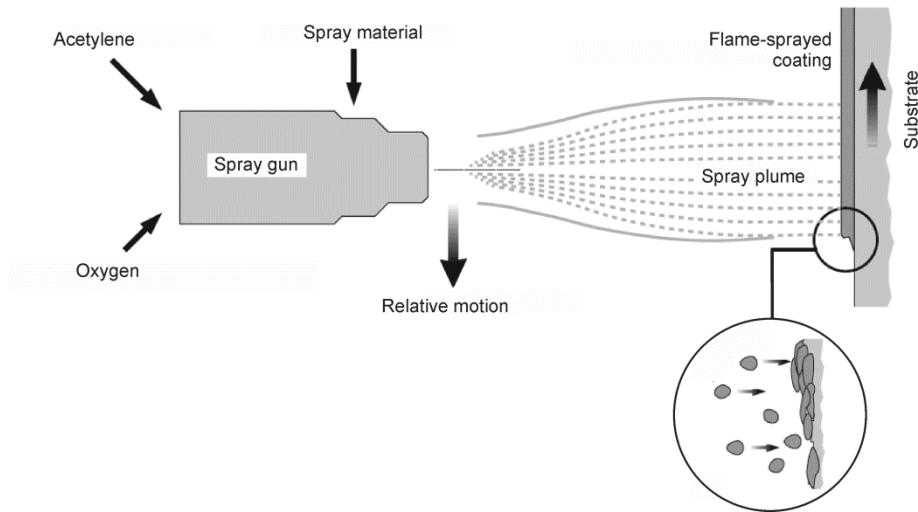


Figure 1.1: Schematic of flame spraying [20]

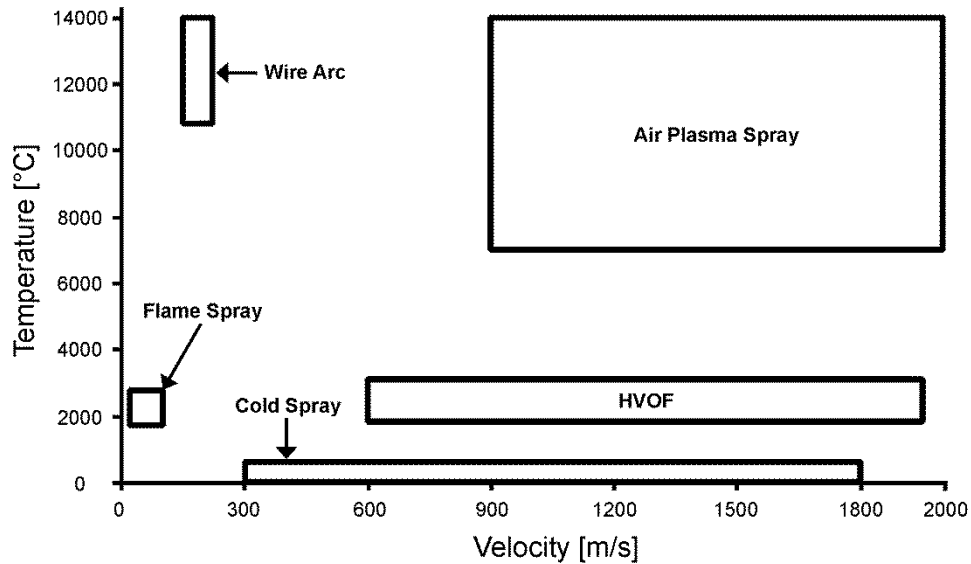


Figure 1.2: Gas temperatures and velocities for various thermal spray processes [21, 22]

With regards to coating a polymer surface, since both the wire arc and plasma spraying processes generate temperatures above 5000°C, and charring of fibreglass polymers occurs at temperatures greater than ≈650°C, these types of processes were not considered further [21, 22, 23]. However, it has been reported that a coating was successfully deposited with plasma spraying on polymer rotor blades, but no details regarding process parameters have been forthcoming [7]. Although cold spraying has a low temperature, the process is not conducive to spray over large areas.

The flame spraying and HVOF processes are very similar. The flame spraying process combusts a mixture of a hydrocarbon fuel, usually acetylene, and oxygen in the torch to melt and accelerate the particles towards the substrate. The molten and semi-molten particles impact the surface of the

substrate, cool and solidify upon impact into splats. The splats form a lamellar coating, with the coating thickness easily controlled by the number of layers deposited. This control over thin layers means that less material is required, which reduces the cost and weight of the final product.

Although the flame spraying and HVOF processes are similar, the HVOF process accelerates particles to high velocities (up to 2000 m/s), much greater than the flame spray process (up to 50 m/s) [21, 22]. The HVOF process achieves such large velocities from confined combustion within an extended nozzle, which heats and accelerates the spray particles before leaving the nozzle. Contrarily, the flame spray process combustion is unconfined, occurring outside of the nozzle, and therefore the spray particles are not accelerated to such large velocities. Due to the increased velocities, the porosity of HVOF coatings, less than 2%, are much less than that of flame-sprayed coatings. Also, the energy input to the substrate, including both thermal and kinetic particle energies is much greater for the HVOF process.

Oxy-acetylene flame spraying is known to have the lowest cost of all thermal spray processes due to the low equipment and operating costs. The gases required, acetylene and oxygen, are commonly found in machine shops. Further, less ancillary equipment, such as chillers for plasma spraying, are required for flame spraying and the flame spraying equipment is much more portable than HVOF or plasma spraying equipment. To coat polymer surfaces, flame spraying has been selected due to its low temperature, low cost, and portability.

1.1.3 Polymers

Polymers, including fiber-reinforced polymers (FRPs) are widely used in many applications. Increasingly, polymer matrix composites (PMC's), which include glass and carbon FRPs, are being used in advanced technology industries due to their light weight, high tensile strength, low cost and high corrosion resistance [24]. However, some of the factors limiting PMC use include flammability, operational temperature and poor erosion resistance [25, 26]. To overcome these limitations, PMC's have incorporated thermally sprayed coating systems that are capable of improving erosion and oxidation resistance under thermo-mechanical loads [26]. As a result, the wear resistance and coating adhesion/cohesion of WC-Co coatings on polymers for aerospace propulsion applications has been well studied [26-29]. With regards to high temperature applications, coatings on PMC's have also been used to act as a thermal shield, with the coating being a low thermal conductivity or high reflectivity material, to protect the PMC material from decomposition [30].

Polymers have also been deposited as coatings. Recently, composite coatings of alumina-titania/fluoropolymer (PTFE or PFA) have been plasma-sprayed to obtain an erosion-resistant low friction coefficient surface [31]. Polymeric coatings have been used as lightweight thin barriers against corrosion [32]. Further, flame-sprayed polyether ether ketone (PEEK) coatings, deposited with a low temperature flame, and re-melted with a carbon dioxide (CO₂) laser have produced a dense and homogenous film [33].

In all cases, the adhesion strength of the polymer coating has been of considerable interest.

An issue with the deposition of metallic coatings onto polymer substrates is coating adhesion on the substrate [34]. To address this issue, preparation of the polymer substrate surface with grit blasting, in a similar method that is used for metallic substrates, has been used to roughen the polymer surface to promote adhesion [35]. For unheated metal substrates, roughened surfaces have been reported to consistently promote improved adhesion and cohesion of coatings [36, 37]. However, it has been reported that grit-blasting can cause fiber damage in PMC's [27, 38]. Therefore, co-curing copper particles into the laminate of carbon/epoxy polymer matrix composites has resulted in successful deposition of metals by pulsed gas dynamic spraying, a form of cold spraying, without the use of grit blast surface preparation [39].

1.2 Previous Studies

Most studies involving polymer-metallic structures fabricated by thermal spraying have focused on the deposition of polymers on metal substrates [40]. Although as previously reported, WC-Co coatings for high temperature and erosion resistance applications on PMC's have been well studied [26-29]. Though there are limited studies of metallic coatings on polymers, metallic coatings have been used as bond coats for erosion resistant coatings. In the 1990s, Chambers *et al.* [41] reported that titanium carbide/nickel alloy (TiC + 10wt.%Ni) and zirconium diboride (ZrB_2) have

been deposited onto polyimide substrates successfully. Later, it was reported that a wire arc-sprayed metallic coating applied to a zinc bond coat on PMC's is suitable for erosion resistance applications [38]. Additionally, Meador *et al.* [42] have used a bond coat made of zinc with the addition of up to 5% polyimide to improve the compatibility between the PMC substrate and top coat for improved erosion properties. In another study, Liu *et al.* [34] also investigated using several different bond coats deposited by arc spraying on carbon fiber reinforced polyimide substrates. In this study, it was reported that zinc and aluminum were suitable bond coats, while nickel and copper were not due to their higher melting points. For thermal barrier coatings, a thin (30 μm) aluminum bond coat has been deposited by atmospheric plasma spray on PMC's successfully [43].

Only recently have studies focused on the deposition of metallic coatings (zinc) on cured carbon fiber epoxy matrix composites with a form of cold spraying [39]. In this study it was found that there was limited fiber damage due to the low process temperatures required, due to the low melting point (419°C) of zinc. Further studies by Gosselin *et al.* [44] have investigated the thermal and mechanical performance of the PMC's coated with copper by cold spraying. In both studies, there was a layer of copper particles co-cured on the surface of the PMC's to promote coating adhesion while preventing fiber damage. Other studies have investigated aluminum metallic and aluminum-copper bimetallic coatings deposited on carbon fiber-reinforced PMC's also by cold spraying that have achieved reasonable bonding [45].

Aluminum coatings have also been flame-sprayed onto polyester textile substrates while using a cooling system [46]. The coatings were used to investigate the electrical conductivity without inducing thermal or chemical damages to the flexible fabric material. Although these coatings were thin (75 μm), it was found that the surface conductivity increased proportionally to the coating thickness.

Preliminary studies reporting functional metallic coatings, for applications other than erosion resistance or bond coat protection, on polymers have only recently been reported. Huonnic *et al.* [40] successfully deposited flame-sprayed aluminum coatings onto grit-blasted glass and basalt fiber reinforced epoxy tubes. The coatings were investigated for electrical conduction to quantify the quality of the coating and mechanical testing to determine degradation from the grit blasting and flame spraying processes. The mechanical testing reported a burst pressure that was 35% lower for coated samples than uncoated control samples, indicating that the coating process significantly reduces structural integrity of the composite structure.

The purpose of this study will be to flame spray a metallic coating onto flat polymer substrates successfully. The coated samples will be characterized to ensure that limited fiber damage occurred, before the heat transfer performance of the coating-composite structures is investigated. In order to quantify heat transfer of the coated polymer structures, surface temperature measurements under forced convection will be taken.

Although there are successful commercial applications [6], the technical literature relating to thermal spraying of metallic coatings on polymer substrates is limited. Further, it should be noted that through discussion with a GKN employee, neither the concept nor method has been patented or published (G. Lunn, personal communication, May 23, 2012). This study aims to contribute to the subject matter while investigating the heat transfer of the composite structure.

1.3 Objectives

The goal of this study was to investigate the heat transfer of a novel metallic coating on a polymer structure. Further, the objective of the deposition of a metal coating onto the polymer-based substrate samples is to minimize hot spots and increase the surface temperature distribution away from the heating wire. To accomplish this goal the following tasks were executed:

1. Fabrication of a thin flame-sprayed coating on glass fiber-reinforced epoxy matrix composites without degradation of the polymer.
2. Characterization of the composite layers' thicknesses, volume fractions and compositions.
3. Use of thermocouples to measure surface temperatures and characterize the heat transfer of the composite structures with insulated and forced convection surfaces.
4. Fabrication and measurement of surface temperatures of polymer-coating-polymer structure with forced convection surfaces.
5. Develop an analytical model to calculate the polymer surface temperatures based on the experimentally measured coating surface temperatures.
6. Develop a numerical model to validate the assumptions and results of the analytical model.

1.4 Thesis organization

Following the introduction in this chapter, the second chapter describes the novel experimental method, which was used to fabricate and evaluate the heat transfer capability of flame-sprayed metal-polymer composite structures. Details are included regarding the different experiments performed to evaluate the assemblies. Chapter 3 presents the data and details the analysis of the experiments. Mathematical and numerical models are included, which were used to estimate the surface temperatures based on the experimental parameters. Chapter 4 offers a conclusion of this study.

1.5 References

1. V. Gray, Prediction of Aerodynamic penalties caused by Ice Formations on Various Airfoils, NASA Technical Note D-2166, NASA, Washington, D.C., USA, 1964, 19 pages.
2. R. Gent, N. Dart, J. Cansdale, Aircraft Icing, Philosophical Transactions: Mathematical, Physical and Engineering Sciences, 2000, 358 (1776), pp. 2873-2911.
3. M. Sinnett, 787 No-bleed Systems: Saving Fuel and Enhancing Operational Efficiencies, AERO Quarterly, 2007, Issue 28, pp. 6-11.
4. R. Gardner, The big boys go for plastic, Aerospace Engineering, SAE International, June 2012, pp. 6-17.
5. M. Mecham, R. Wall, Ice Spray, Aviation Week & Space Technology, Nov. 22, 2010, 172(42), pp. 16.
6. J. Sloan, 787 integrates new composite wind de-icing system, High Performance Composites, 2009, 17(1), pp. 27-29.
7. B. Rooks, Robot Spraying of Helicopter Rotor Blade Ice Protection System, Industrial Robot, 2001, 28(4), pp. 313-315.
8. O. Parent, A. Ilinca, Anti-icing and de-icing techniques for wind turbines: Critical review, Cold Regions Science and Technology, 2011, 65, pp. 88-96.
9. F. Richert, Is Rotorcraft Icing Knowledge Transferrable to Wind Turbine?, BOREAS III, FMI, Saariselka, Finland, pp. 366-380.

10. A. Ilinca, Analysis and Mitigation of Icing Effects on Wind Turbines, Wind Turbines, 2011, Ibrahim Al-Bahadly (Ed.), InTech, pp. 177-214.
11. E. Eckert, Survey on heat transfer at high speeds, United States Air Force, 1961.
12. J. Kaye, The Transient Temperature Distribution in a Wing Flying at Supersonic Speeds, M.I.T. Division of Industrial Cooperation, 1949, pp. I, 34.
13. J. Kaye, Survey of Friction Coefficients, Recovery Factors, and Heat Transfer Coefficients for Supersonic Flow, Journal of Aeronautical Sciences, 21 (1954) 117-129.
14. L. Jiji, Heat Conduction, third ed., Springer, Inc., New York, 2009, pp. 2-8, 36.
15. P. Oosthuizen, D. Naylor, An Introduction to Convective Heat Transfer Analysis McGraw-Hill, Inc., New York, 1999, pp. 1-5.
16. G. Nellis, S. Klein, Heat Transfer, Cambridge University Press, Ltd., New York, 2009, pp. 485, 491, 509, 542, 547.
17. H. Schlichting, Boundary-Layer Theory, seventh ed., McGraw-Hill, Inc., New York, 1979, pp. 298.
18. A. Zhukauskas, A. Ambrazyavichyus, Heat transfer of a plate in a liquid flow, Int. J. Heat Mass Transfer, 3 (1961) 305-309.
19. A. Shapiro, The Dynamics and Thermodynamics of Compressible Fluid Flow, 2 vols., Ronald Press Co., New York, 1953, pp. 211-212, 1071, 1123.

20. "An Introduction to Thermal Spray", Sulzer Metco Inc., 2012. [Online] Available: www.sulzer.com/en/Products-and-Services/Coating-Equipment/Thermal-Spray [Accessed October 29, 2012].
21. Handbook of thermal spray technology, ASM International, Thermal Spray Society Training Committee, 2004, ASM, pp. 5-9.
22. P. Fauchais, G. Montavon, Thermal and cold spray: recent developments, Key Engineering Materials, 2008, 384, pp. 1-59.
23. A. Mouritz, S. Feih, E. Kandare, Z. Mathys, A. Gibson, P. Des Jardin, S. Case, B. Lattimer, Review of fire structural modelling of polymer composites, Composites: Part A, 2009, 40, pp. 1800-1814.
24. ASM Handbook, Volume 20, Materials Selection and Design, Properties versus Performance of Materials, Design with Plastics.
25. H. Zhang, Fire-Safe Polymers and Polymer Composites, U.S. Department of Transportation, Federal Aviation Administration, 2004, p. 1-1.
26. M. Ivosevic, R. Knight, S. Kalidindi, G. Palmese, J. Sutter, Solid Particle Erosion Resistance to Thermally Sprayed Functionally Graded Coatings for Polymer Matrix Composites, Surface & Coating Technology, 2006, 200(16), pp. 5145-5151.
27. M. Ivosevic, R. Knight, S. Kalidindi, G. Palmese, J. Sutter, Adhesive/Cohesive Properties of Thermally Sprayed Functionally Graded Coatings for Polymer Matrix Composites, Journal of Thermal Spray Technology, 2005, 14(1), pp. 45-51.
28. J. Sutter, K. Miyoshi, C. Bowman, S. Naik, K. Ma, R. Sinatra, R. Cupp, R. Horan, G. Leisler, Erosion Coatings for Polymer Matrix

- Composites in Propulsion Applications, High Performance Polymer, 2003, 15(4), pp. 421-440.
29. K. Miyoshi, J. Sutter, R. Horan, S. Naik, R. Cupp, Assessment of Erosion Resistance of Coated Polymer Matrix Composites for Propulsion Applications, Tribology Letters, 2004, 17(3), pp. 377-387.
 30. J. Brossas, Fire retardance in polymers: An introduction lecture, Polymer Degradation and Stability, 1989, 4(23), pp. 313-325.
 31. C. Mateus, S. Costil, R. Bolot, C. Coddet, Ceramic/Fluoropolymer Composite Coatings by Thermal Spraying – a Modification of Surface Properties, Surface & Coating Technology, 2005, 191(1), pp. 108-118.
 32. V. Lins, J. Branco, F. Diniz, J. Brogan, C. Berndt, Erosion Behavior of Thermal Sprayed, Recycled Polymer and Ethylene-Methacrylic Acid Composite Coatings, Wear, 2007, 262(3), pp. 274-281.
 33. G. Zhang, H. Liao, H. Yu, S. Costil, S. Mhaisalkar, J.-M. Bordes, C. Coddet, Deposition of Peek Coatings Using a Combined Flame Spraying-Laser Remelting Process, Surface & Coating Technology, 2006, 201(1), pp. 243-249.
 34. A. Liu, M. Guo, J. Gao, M. Zhao, Influence of Bond Coat on Shear Adhesion Strength of Erosion and Thermal Resistant Coating for Carbon Fiber Reinforce Thermosetting Polyimide, Surface & Coating Technology, 2006, 201(6), pp. 2696-2700.
 35. U. Diccar, “Plasma Spray Coatings for Polymer Composites”, MSc Thesis, Wichita State University, 2006, pp. 37.

36. M. Mellali, P. Fauchais, A. Grimaud, Influence of Substrate Roughness and Temperature on the Adhesion/Cohesion of Alumina Coatings, *Surface & Coating Technology*, 1996, 81(2-3), pp. 275-286.
37. S. Amada, T. Hirose, Influence of Grit Blasting Pre-Treatment on the Adhesion Strength of Plasma-Sprayed Coatings: Fractal Analysis of Roughness, *Surface Coating Technology*, 1998, 102(1-2), pp. 132-137.
38. A. Liu, M. Guo, M. Zhao, H. Ma, S. Hu, Arc-Sprayed Erosion-Resistant Coating for Carbon Fiber Reinforced Polymer Matrix Composite Substrates, *Surface & Coating Technology*, 2006, 200(9), pp. 3073-3077.
39. F. Robitaille, M. Yandouzi, S. Hind, B. Jodoin, Metallic Coating of Aerospace Carbon/Epoxy Composites by the Pulsed Gas Dynamic Spraying Process, *Surface & Coating Technology*, 2009, 203(19), pp. 2954-2960.
40. N. Huonnic, M. Abdelghani, P. Mertiny, A. McDonald, Deposition and characterization of flame-sprayed aluminum on cured glass and basalt fiber-reinforced epoxy tubes, *Surface & Coatings Technology*, 2010, 205, pp. 867-873.
41. D. Chambers, K. Taylor, C. Tan, A. Emrick, Sputtering on Polymeric Composites, *Surface & Coating Technology*, 1990, 41(3), pp. 315-323.
42. M. Meador, J. Sutter, G. Leissler, E. Shin, L. McCrokke, Coatings for High Temperature Polymer Composites, *International SAMPE Symposium and Exhibition*, 2001, pp. 572-585.
43. W. Huang, X. Fan, Y. Zhao, X. Zhou, X. Meng, Y. Wang, B. Zou, X. Cao, Z. Wang, Fabrication of thermal barrier coating onto polyimide

matrix composites via air plasma spray process, *Surface & Coating Technology*, 2012, 207, pp. 412-429.

44. S. Gosselin, F. Robitaille, B. Jodoin, M. Yandouzi, Characterization of cold sprayed copper coatings for carbon fibre/epoxy composite moulds, *Proceedings - American Society for Composites*, 2011, 3, pp. 2243-2258.
45. X. Zhou, A. Chen, J. Liu, X. Wu, J. Zhang, Preparation of metallic coatings on polymer matrix composites by cold spray, *Surface & Coatings Technology*, 2011, 206, pp. 132-136.
46. J. Voyer, P. Schulz, M. Schreiber, Electrically Conductive Flame-Sprayed Aluminum Coatings on Textile Substrates, *Journal of Thermal Spray Technology*, 2008, 17(5/6), pp. 818-823.

Chapter 2 Experimental Method

This experimental procedure was developed to investigate the heat transfer through metallic coatings flame-sprayed on polymer flat plates. Samples were prepared for three experiments, where the coating and polymer surface temperatures were measured. The first experiment, to demonstrate the applicability of the concept, consisted of thin polymer samples with an aluminum-12silicon (Al-12Si) coating. A resistive heating wire was mounted to the leading edge of the coating surface, while both the coating and polymer surfaces were insulated. Thicker polymer samples were prepared, which were then coated in the same manner. These samples were mounted in a high speed wind tunnel, heated in a similar manner and the temperature variation between the coating and polymer surface was studied. Finally, the coated thick polymer samples had a final top layer of glass fiber-epoxy wound above the coating to protect it from oxidation and erosion while the temperature variations were examined. The experimental method explains the polymer fabrication, flame spraying, coating characterization, and the methodology to heat the samples and measure their temperatures.

2.1 Polymer Fabrication

Glass fiber-reinforced epoxy flat plates were fabricated using a filament winding machine (WMS-4 Axis, McClean-Anderson, Schofield, WI, USA). Bisphenol-A epoxy was combined with a non-MDA polyamine hardener

to form the resin system (EPON826-EPICURE9551, Hexion Specialty Chemical, Columbus, OH, USA). The resin was heated to 30°C in a drum-type resin bath. Five glass strands, each with a linear weight of 1.1 g/m, were impregnated as they passed over the drum (158B Type 30, Owens-Corning, Toledo, OH, USA). The impregnated glass fibers passed through the pay-out eye before being wound at $\pm 60^\circ$ around the rectangular shaped mandrel, which was rotated at up to 20 RPM. Note that the polymer-coating-polymer samples had a single top layer of fibers wound at 90° . All fibers were kept in tension, with a target tension per fiber of 15.6 N, but the tension varied slightly due to the rectangular shaped mandrel (ETS-6E-10, McClean-Anderson, Schofield, WI, USA). The tensioning system and resin bath are shown in Fig. 2.1. The thin specimens consisted of two fiber layers, while the thicker samples consisted of eight fiber layers, with each layer consisting of ten passes. A foam brush was used to remove excess resin during winding. Following winding, the brush ensured that there was a thin but uniform surface layer of resin. Prior to curing, a tea strainer was used to deposit a 220 grit fine garnet sand ($\sim 63\mu\text{m}$) layer uniformly on the thin epoxy layer (220 HPX Garnet Sand, Barton International, Glen Falls, NY, USA). An infrared heater was used to heat the polymer for approximately two hours while the mandrel was rotated as shown in Fig. 2.2. The resin rose to the surface during curing, which required that garnet sand be reapplied after 45 minutes of heating to obtain a rough garnet sand-epoxy matrix top surface. Once fully cured, the samples were removed from the mandrel with an angle grinder and a tile saw was used to cut samples with dimensions of 90 mm by 120 mm.



Figure 2.1: Image of the tensioning system and resin bath

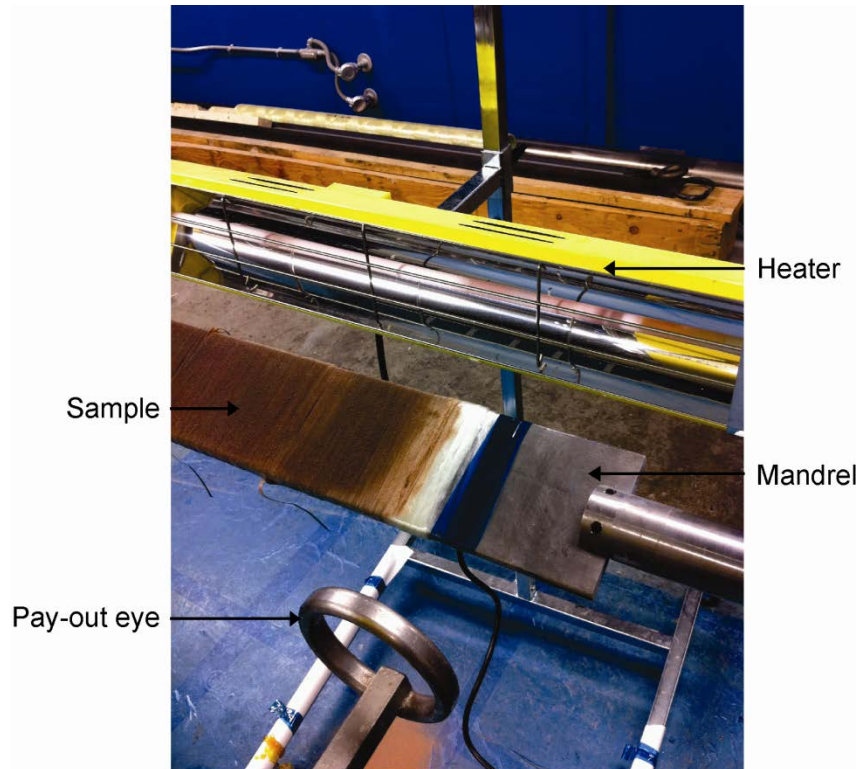


Figure 2.2: Image of polymer fabrication

2.2 Flame Spraying

An oxy-acetylene flame spray torch (6P-II, Sulzer Metco, Westbury, NY, USA) was used to deposit an aluminum-silicon (88 wt. % aluminum-12 wt. % silicon, Al-12Si) powder (52C-NS, Sulzer Metco, Westbury, NY, USA). The particle sizes varied between 45 μm and 90 μm (-90+45 μm). A volumetric powder feeder (5MPE, Sulzer Metco, Westbury, NY, USA) used argon as the carrier gas to transport the powder to the flame spray torch. The argon gas flow rate was 7 normal liters per minute (NLPM), at a gauge pressure of 414 kPa (60 psig), and the volumetric powder feeder was set to a powder feed rate of 60 flow meter reading (FMR). A combustion flame was generated from the torch by supplying acetylene and oxygen at 6 and 20 (NLPM), respectively. Compressed air at 35 kPa (5 psig) was introduced into the oxygen-rich flame to provide cooling and accelerate the particles.

The substrate was held stationary and the flame spray torch was attached to a robot (HP-20, Motoman, Yaskawa Electric Corp., Waukegan, IL, USA) to ensure control and repeatability of the spray parameters. The samples were fixed length-wise since orienting the substrates along the shorter dimensions resulted in distortion due to the heat generated from flame spraying. The distance between the torch and substrate (stand-off distance) was 150 mm. The linear velocity of the torch was 500 mm/s. The increment, the distance that the robot moves up between depositions of a single line of coating, was set to 2 mm. To obtain the desired thickness, the torch made two or three passes; however, there was a two minute pause

between passes to let the samples cool. The compressed gas lines, flame spray torch, and the polymer substrate are shown in Fig. 2.3. Note that the substrates were not pre-heated before deposition of the coating.

Following flame spraying, a top polymer layer was wound above the coating of some of the samples. This layer was prepared in a similar manner as described before, except that the winding angle was approximately 88° , as opposed to $\pm 60^\circ$, and only one layer of fibers was wound. The purpose of this thin polymer layer was to protect the coating, while not impeding heat transfer. Table 2.1 shows the number of layers of fibers and metal coating that were used to fabricate the composite structures.

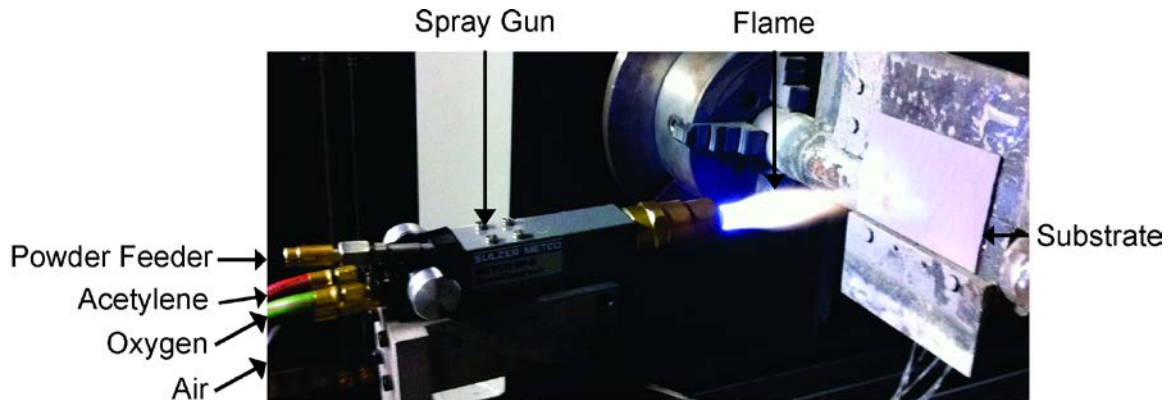


Figure 2.3: Image of flame spraying polymer substrate

Table 2.1: Number of layers of fibers and passes during flame spraying

Test name	Layers of fibers - Polymer Base	Number of passes - Flame Spraying	Layers of fibers - Polymer Top
Insulated Tests	2	2	N/A
Wind Tunnel – Test #1	8	2	N/A
Wind Tunnel – Test #2	8	3	1

2.3 Coating Characterization

After flame spraying, the samples were cut into 13 mm x 13 mm sections for X-ray diffraction (XRD) analysis to identify the phases in the coating. The instrument was a rotating anode XRD system equipped with a copper anode (Rigaku RU-200B, Rigaku Americas, The Woodlands, TX, USA). The scan speed was continuous at 3 degrees per minute in thin film mode. A curved graphite monochromator was used and the power was set to 40 kV and 110 mA.

Flame-sprayed samples were cold-mounted for cross-sectional microstructural analysis to determine the porosity and thickness of the coating. The samples were cold-mounted in epoxy and due to the samples and epoxy having similar density; weights had to be attached to the samples such that they remained on the bottom surface of the epoxy. The epoxy-mounted

samples were ground, polished to a 1 μm diamond finish and prepared for scanning electron microscopy (SEM) equipped with energy-dispersive x-ray spectroscopy (EDX) (Zeiss EVO MA 15, Carl Zeiss NTS - LLC, Peabody, MA, USA). The microscope was operated in back scattered electron mode to generate images and EDX was used to provide the quantitative amount of the elements found using XRD.

2.4 Heating and Temperature Measurement

The coating-polymer composite samples were heated with a resistance heating wire. A DC power supply (Model 1692, BK Precision, Yorba Linda, CA, USA) was used to generate a current. The voltage drop across the heating wire and current were measured using multi-meters (HHM14, Omega Engineering Inc., Stamford, CT, USA) to determine the electrical power. The electrical circuit and components are shown in Figs. 2.4 and 2.5, respectively.

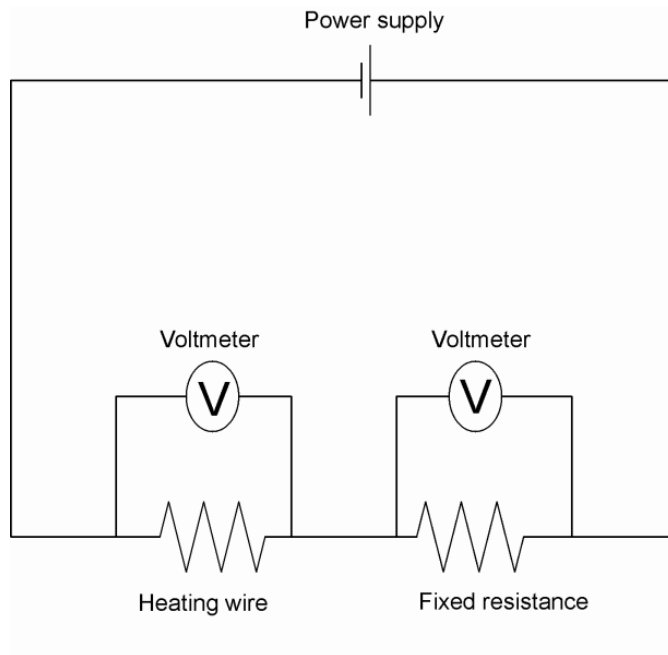


Figure 2.4: Schematic of the electrical circuit

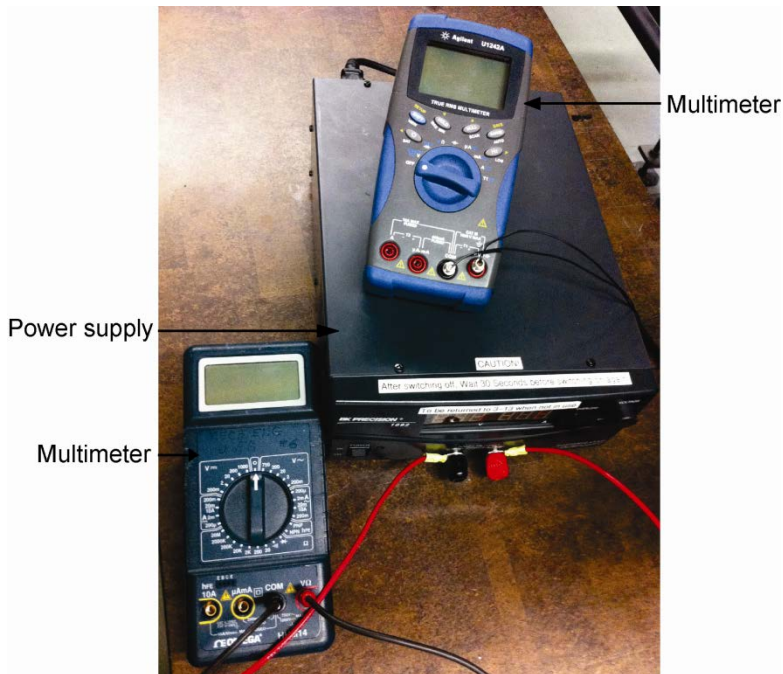


Figure 2.5: Image of the electrical components

The heating wire on the insulated samples was wrapped with Teflon tape to prevent electrical current from flowing through the metallic coating. The Teflon was thin, highly conformable, electrically insulating and had a high thermal conductivity [1]. Thermocouples (Type K thermocouple, Wika Instruments Ltd., Edmonton, AB, Canada) were used to measure the surface temperatures of the metallic coating and polymer. The thermocouples were attached at eight locations on both the metallic coating and polymer surfaces. As measured from the resistive heating wire, the locations were between 0 mm and 50 mm, inclusive, and in 10 mm increments. Thereafter, thermocouples were located at 75 mm and 100 mm from the heating wire. The thermocouple wire junctions were flattened in a press in order to achieve better thermal contact with the rough coating surface. Figure 2.6 shows an image of the coated sample with the Teflon-wrapped heating wire and thermocouples on the coated surface. Wall mounting tabs with foam backings were used to attach the thermocouples to the surfaces, since the foam contracts under heat and thus promotes thermocouple contact beneath the foam. The thin samples were compressed between two pieces of extruded Styrofoam to provide insulation and restrict heat loss.

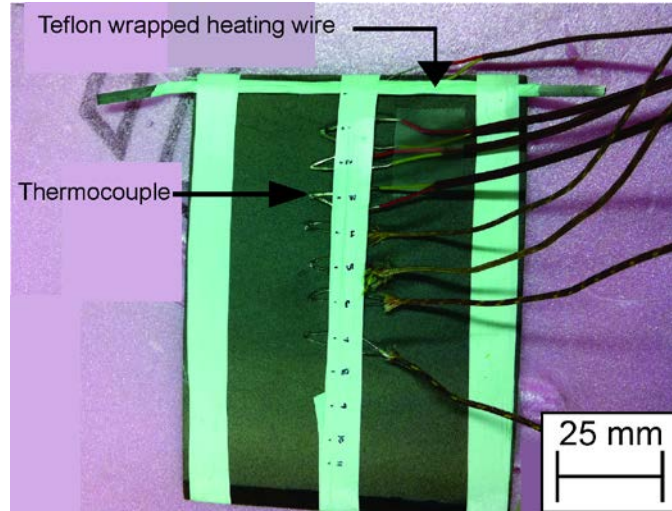


Figure 2.6: Image of coated polymer plate for insulated tests

For the wind tunnel tests, a thin polyimide tape was applied to the heating wire to prevent electrical current from flowing through the metallic coating (3M541312, Digi-Key Corporation, Thief River Falls, MN, USA). Although the Teflon tape would also be effective for this purpose, the tape vibrated at high wind speeds. The polyimide tape was 0.069 mm thick with a 0.043 mm thick silicone thermosetting adhesive that was chosen due to its conformability, high maximum operating temperature, dielectric strength and relatively high thermal conductivity [2]. The wind tunnel tests used Type T thermocouples (Omega Engineering Inc., Stamford, CT, USA) which were also flattened and attached at the same locations as the insulated experiment. However, the thermocouples were attached using a conductive epoxy (Silver Conductive Epoxy, MG Chemicals, Surrey, BC, Canada) along the coating surface and a strain gauge adhesive (M-Bond 610, Vishay Precision Group, Wendell, NC, USA) along the polymer surface. Note that

neither adhesive could be cured above 100°C since prolonged heat denatures the polymer epoxy.

The samples were mounted rigidly in the wind tunnel as shown in Fig. 2.7. Symmetrical support plates were fabricated, where each had two clamps near the leading edge for the heating wire, two holes for short welding rods and two mounting holes. The mounting bolts held the support plate while also allowing the current to flow through them. The current then flowed through the support plates and across the heating wire which was clamped at the sample's leading edge. There were four holes drilled into the thick electrically insulating polymer layer through which the samples were supported with welding rods. Rigid insulation was inserted on the welding rods between the samples and the aluminum support plates inside the wind tunnel (Superwool Fibre, Morgan Thermal Ceramics, 55-57 High St., Windsor, Berkshire, UK). A small aluminum airfoil was attached along the front face such that there was no flow separation. Although this airfoil was noticeably warmer at the conclusion of the experiment, once steady state was reached, there would be no heating flux since this surface is not in the air. Due to the slight curvature of the samples from winding, the tension on the heating wire kept it in constant contact with the coating. By varying the distance between the support plates with tension rods, the thermal expansion in the heating wire could be accommodated so that there was constant tension on the heating wire. The wind tunnel was run at or near the maximum wind speed of approximately 28 m/s. The free stream air speed was measured with a Pitot tube connected to a pressure transducer. The pressure transducer was calibrated with both a digital manometer (922 micro-

manometer, Fluke Corporation, 6920 Seaway Blvd., Everett, WA, USA), and also an inclined red oil filled manometer.

In all the experiments, the temperatures were measured at 1 Hz and for up to 30 minutes. The data from up to 16 thermocouples were collected simultaneously by using a data acquisition system (SCXI-1000, National Instruments, Austin, TX, USA) connected to a personal computer. The data acquisition system input modules (SCXI-1112) provided cold junction compensation such that the temperatures could be measured accurately at any room temperature.

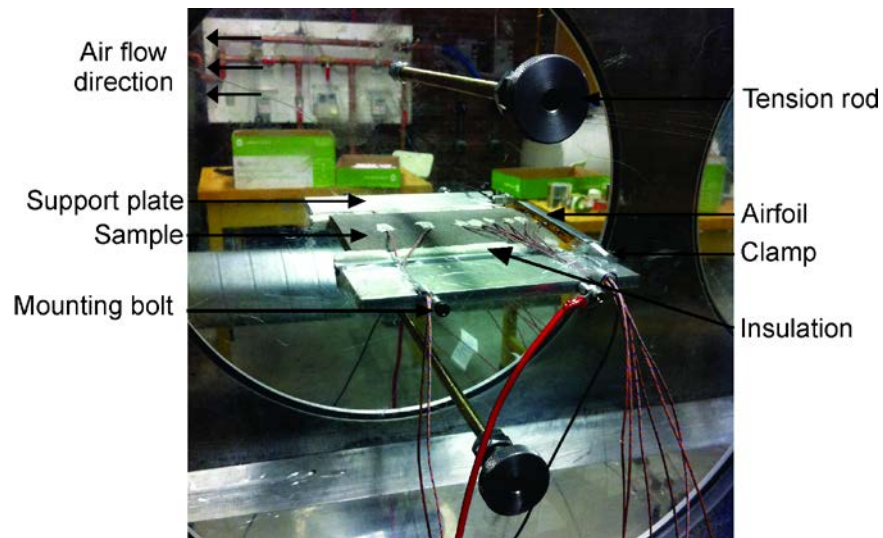


Figure 2.7: Image of embedded metallic coating for wind tunnel tests

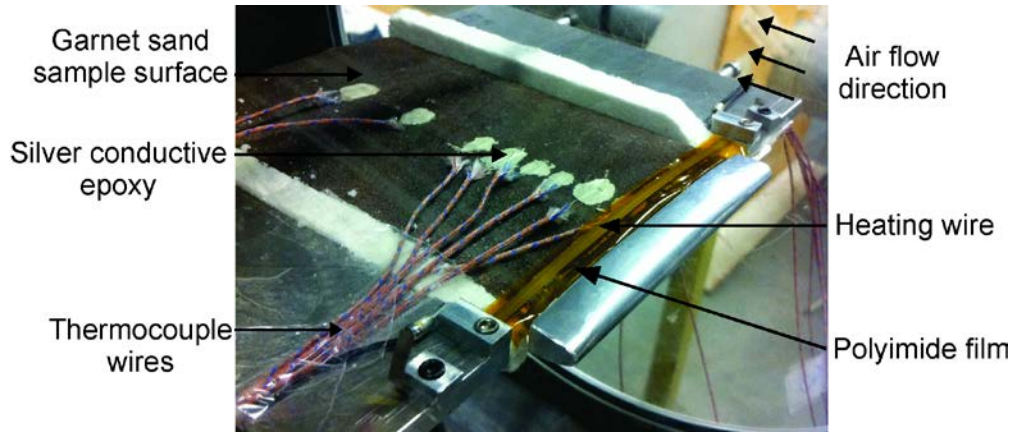


Figure 2.8: Image of the control experiment

A second experiment, which was identical to the first, was performed with a control sample to compare the effect of the coating on surface temperatures. The control sample was a polymer flat plate with a garnet sand surface that was devoid of metallic coating. Figure 2.8 shows a close-up of the control surface as well as the same heating wire power and flux which were used for the coated samples.

2.5 Numerical Method

A finite element analysis (FEA) model was used to validate the experimental and analytical results. The numerical model was built using Solidworks 2012 - Thermal Simulation (Dassault Systemes Solidworks Corp., Waltham, Ma, USA). The input geometry was identical to the specimens fabricated for the first and second wind tunnel tests as summarized in Table 2.2. The length and widths of all layers were set to 10 cm. As will be shown in

the analysis, due to similarity of properties, the polymer and garnet sand layers were treated as one complete polymer layer. The boundary conditions along the width of the specimens were set to zero flux, similarly to the insulation along the specimen sides in the wind tunnel. Due to the small area along the front and rearward faces, the heat lost from these areas was neglected, and the heat flux was also set to zero. The convection along both the top and bottom surfaces was specified by way of the adiabatic wall temperature (T_{aw}) and heat transfer coefficient (h). For the first wind tunnel test, the heating power was specified along the leading face of the coating and set to 50% of the total power (half went into sample, half into air) that was used in the experiments. For the second wind tunnel test, the flux was also specified along the leading face of the coating, but the entire power was specified since the heating wire was located between polymer layers.

Table 2.2: Summary of geometry for numerical analysis

Test	Layer	Thickness [mm]
First wind tunnel	Coating	0.34
	Polymer	9.2
Second wind tunnel	Top polymer	0.9
	Coating	0.51
	Bottom polymer	9.2

2.6 References

1. “Fluoropolymers, Properties and Characteristics of Engineering Plastics and Elastomers”, ASM Engineered Materials Handbook, Vol. 3, ASM International
2. “Secondary Adhesive Bonding of Polymer-Matrix Composites, Selection Criteria”, ASM Handbook, Vol. 21 - Composites, ASM International

Chapter 3 Results and Discussion

3.1 Coating Characterization

Previous studies have shown that grit blasting can enhance the adhesion of flame-sprayed metallic coatings to polymer tubes [1]. However, the present study found that flame-spraying on glass fiber-reinforced epoxy flat plate substrates, with varying levels of roughening by grit blasting, did not create a surface to which the metallic coatings could adhere. Embedding 220 grit fine garnet sand within the epoxy, as the polymer cured, improved coating adhesion following flame spraying. Avoiding grit blasting also reduced the risk of damaging the glass fibers and adversely affecting polymer structural integrity. It should also be noted that sand has been added to pipelines to improve the stiffness of the pipes significantly with a minimal increase in cost [2]. Figure 3.1 shows an image of the coated polymer plate sample.

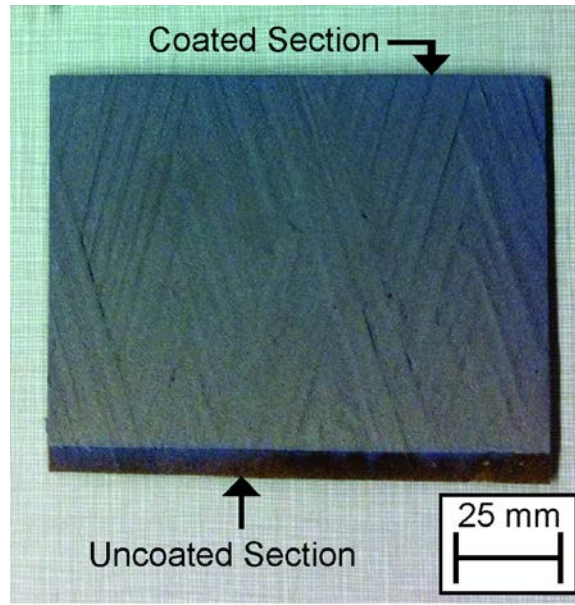


Figure 3.1: Image of coated polymer plate

The metallic coatings consisted of a thin layer of Al-12Si deposited on the garnet sand-roughened surface of the polymer composite. Note that sample preparation was difficult due to the hard garnet sand particles in a soft epoxy matrix and the smearing of the soft metallic coating. Therefore, an auto-polisher was used to prepare the surface to a 1 μm diamond finish. Figure 3.2 shows an SEM image of the cross-section of the aluminum-silicon coating on the polymer composite substrate. Figure 3.3 is at a higher magnification such that it is evident that the coating layer is porous with spherical particles that were likely un-molten or partially molten during deposition. However, the particles and splats were connected, which permitted heat flow within the coating. The porosity in the coating is expected since McDonald *et al.* [3] have shown that partially molten particles may fragment or induce fragmentation of fully molten particles during

spreading, which increases the porosity of the final coating. Visible in the polymer layer is the glass fiber reinforcement. The thicknesses of the layers and volume fractions of the coating, garnet sand, and polymer based substrates were measured and are summarized in Table 3.1 below. It should be noted that the polymer thickness is that of one complete pass of filament winding and the coating thickness was obtained after only one pass of flame spraying. The coating thickness was on the same order as that fabricated by Huonnic *et al.* [1]. The coating thickness is notably lower than that of the garnet sand and polymer composite plate. Note that the standard error of the mean, calculated by dividing the standard deviation by the square-root of the number of samples, is shown with the averages [4]. The standard errors of the mean will be reported with the averages of all other parameters mentioned in this characterization portion of the study.

Table 3.1: Thickness and volume fractions of the layers

Layer	Thickness	Volume Fractions/Coating Porosity
Coating	$172 \pm 14 \mu\text{m}$	$21.8 \pm 0.3 \%$
Garnet sand	$598 \pm 30 \mu\text{m}$	$54.9 \pm 0.9 \%$
Polymer base	$605 \pm 43 \mu\text{m}$	$61.3 \pm 1.5 \%$

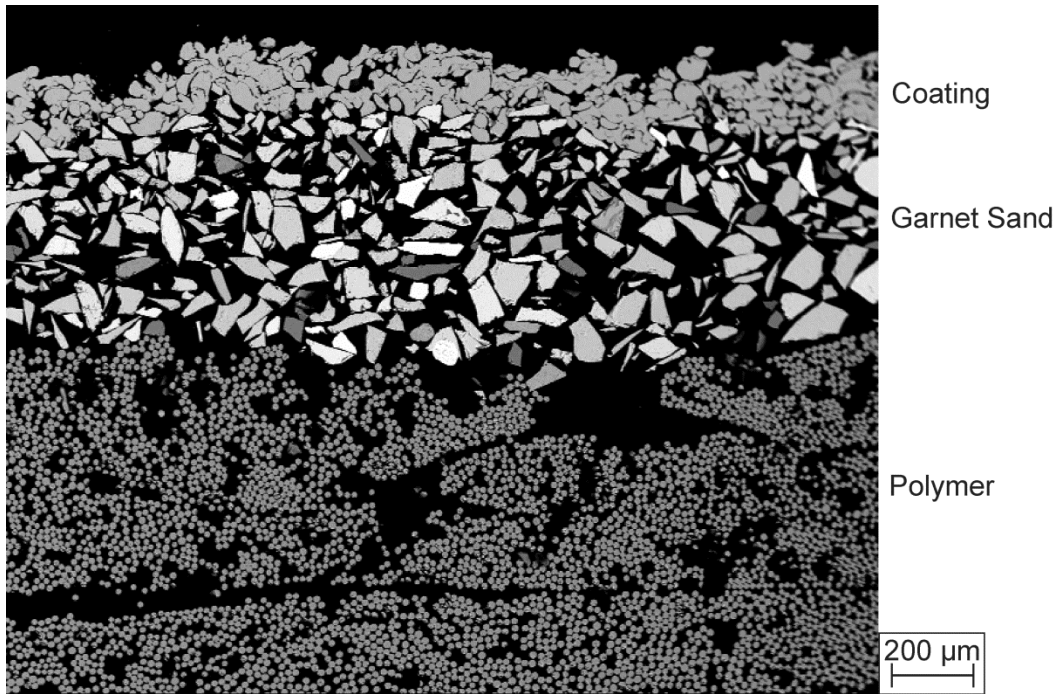


Figure 3.2: SEM image of coating on garnet sand-polymer composite substrate

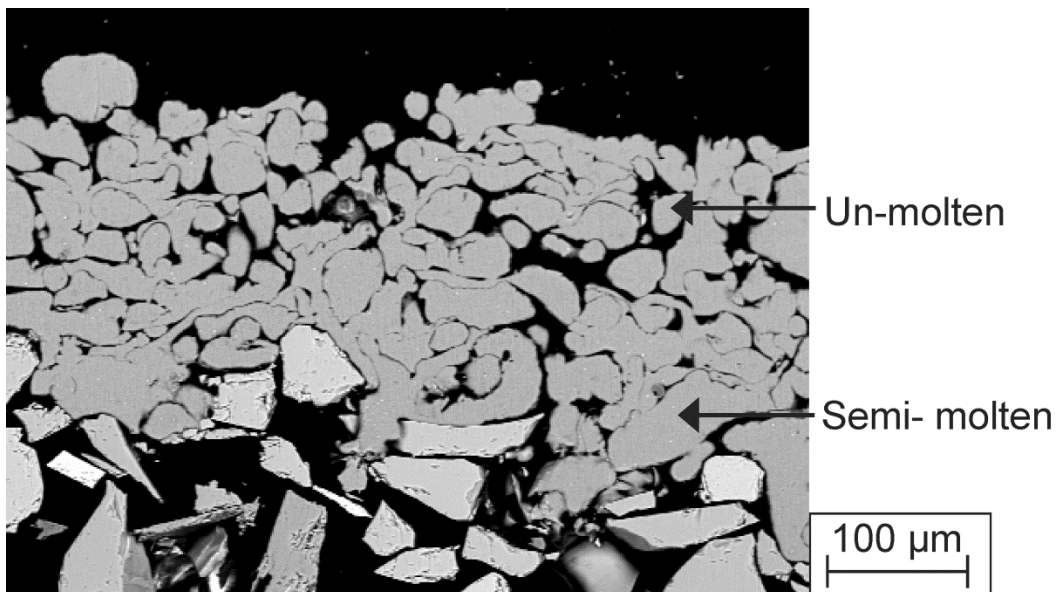


Figure 3.3: SEM image of un-molten and semi-molten coating particles

In order to determine the elemental composition of the coating, elemental mapping was done on the SEM images in order to verify the composition of the coating. EDX (Energy Dispersive Spectroscopy) was used on the coating, garnet sand and polymer layers and the EDX mapping results are shown in Fig. 3.4. From the results of Fig. 3.4, it is important to note that the oxygen content in the coating is very low, indicating that there was probably no oxidation occurring during flame spraying (see Fig. 3.4d). Also note that Fig. 3.4c and e indicate that the coating is composed of aluminum and silicon as the Al-12Si powder was. Point EDX results indicate that the coating is composed of roughly 83.5% aluminum, 10.0% silicon and 6.5% oxygen. The mapping results shown in Fig. 3.4b, c, d and f indicate predominately iron, silicon and oxygen, with trace amounts of calcium in the garnet sand layer. Since garnet sand is made up mostly of almandine minerals ($\text{Fe}_3\text{Al}_2\text{Si}_3\text{O}_{12}$) with some varieties of calcium minerals the EDX results agree well with the expected composition of garnet sand. Although the mapping results do not indicate aluminum, it was present in the point EDX results. From Fig. 3.4b to d the polymer has calcium, silicon and oxygen present. The glass fibers are expected to be predominately silica (SiO_2) and calcium oxide (CaO) explaining the occurrence of these elements.

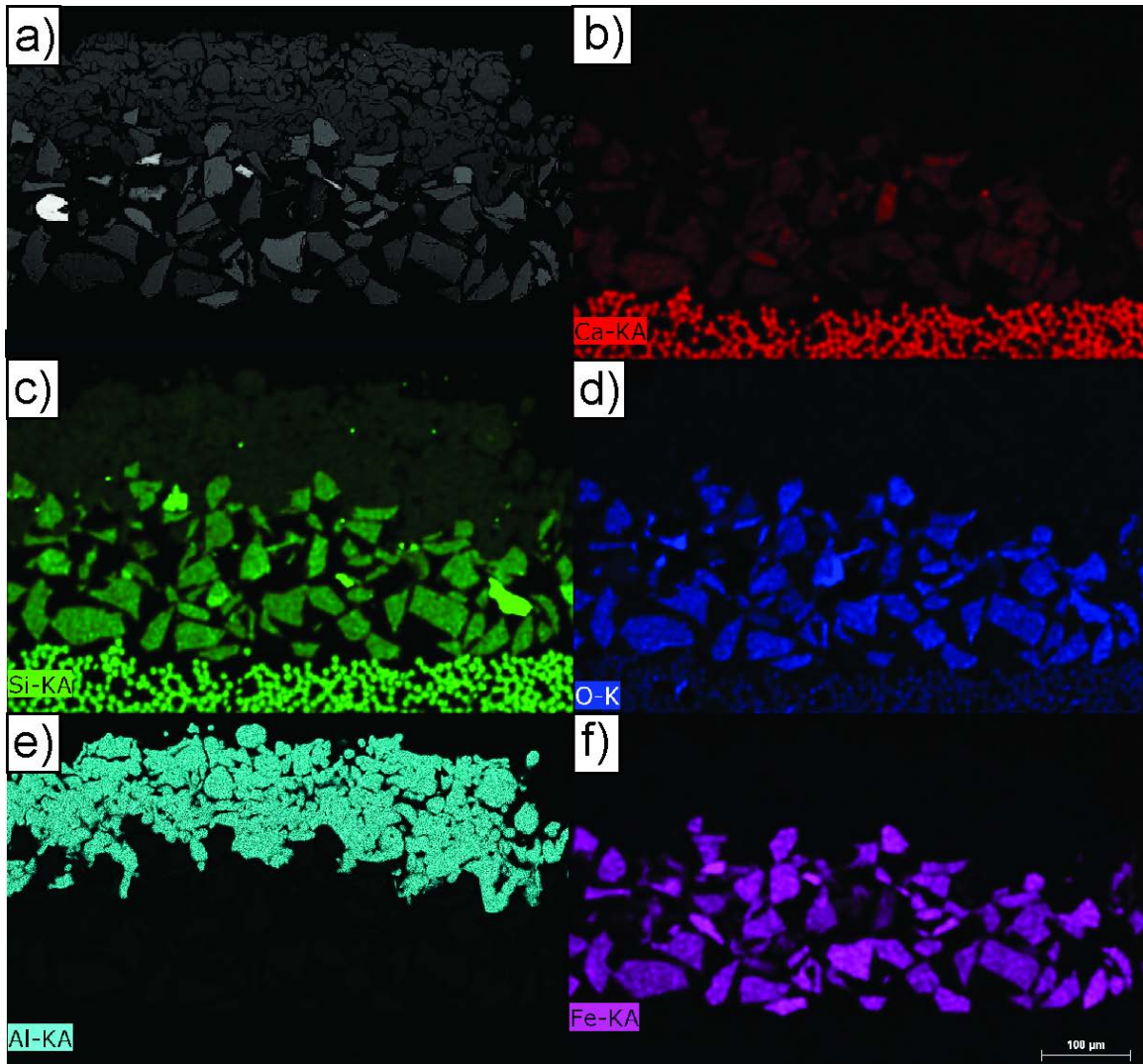


Figure 3.4: Magnification (250x) of a) coating on garnet sand-polymer composite substrate and with EDS mapping for b) Calcium (Ca), c) Silicon (Si), d) Oxygen (O), e) Aluminum (Al) and f) Iron (Fe)

Figure 3.5 reveals the phases present in the coating. The XRD pattern indicates that aluminum and silicon are present. More importantly, this profile does not indicate the presence of aluminum oxide (Al_2O_3). Although the SEM image showed semi-molten particles (see Fig.3.3), this XRD result confirms the result from EDS mapping, that no oxidation occurred during flame spraying. This result is important since the thermal conductivities of the pure metals are generally much greater than the thermal conductivities of metal oxides [5].

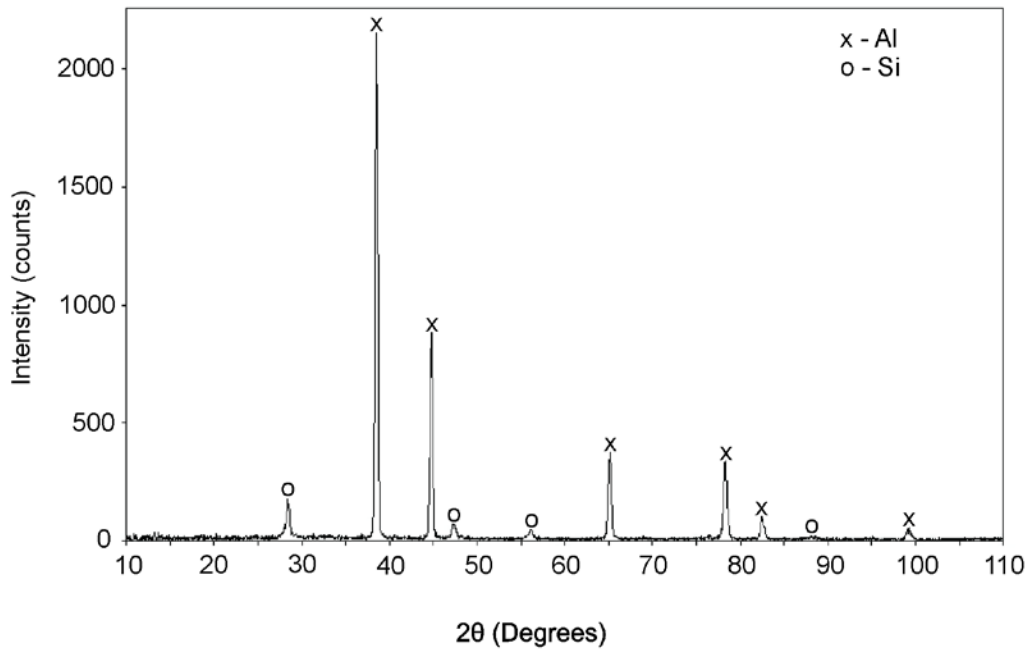


Figure 3.5: XRD pattern of the coating

3.2 Investigation of Fiber Damage

It has been reported that GFRPs first begin to deteriorate by matrix decomposition at roughly 300°C [6, 7]. Roughly 20°C higher, the thermal response of the composite is char formation [6]. The SEM image shown in Fig. 3.2 is of the GFRP cross-section after flame spraying. Importantly, the glass fibers appear the same both near and away from the garnet sand layer, indicating that there is no fiber damage near the garnet sand layer. Figure 3.6 shows a GFRP that was damaged by fire. The fibre char region is nearest to the surface and shown in Fig. 3.6a. Although delamination cracks occur at greater distances from the heated surface than matrix decomposition, the matrix decomposition effects are very obvious and are shown in Fig. 3.6c. Neither delamination cracks nor the decomposition region, shown in Figs. 3.6d and 3.6c, resembles the cross-section of the GFRP sample shown in Fig. 3.2, indicating that heat damage has not occurred.

Temperature measurements along the front garnet sand and the rear polymer surfaces were taken during flame spraying and are shown in Fig. 3.7. In order to determine the polymer thickness at which the matrix decomposition temperature is reached, thin samples (1.8 mm) were used. The temperature along the rear polymer surface of these 1.8 mm thick samples is noticeably higher than that of the 9.2 mm thick samples used in the wind tunnel tests. During flame spraying, the highest temperature is observed at the top of the sample. Therefore, the thermocouples were mounted 5 mm from the top of the samples.

The results from Fig. 3.7 indicate that the maximum garnet sand surface temperature of 440°C is in the range of matrix decomposition temperatures (\approx 300°C to 700°C). Although the temperature at the garnet sand surface is above the matrix decomposition temperature, no char formation or other heat effects were observed, which is further evidenced by SEM images as noted above (see Fig. 3.2). Along the rear polymer surface, the maximum measured temperature of 260°C is below the decomposition temperature indicating that matrix decomposition is definitely not occurring at this location. Therefore for thicker samples, it is expected that there is not any matrix decomposition more than 1.8 mm from the surface. Further, note that a lower temperature is expected in the structural glass fiber layer than on the rough garnet sand surface since the thickness (0.6 mm thick) and low thermal conductivity (0.97 W/m°C, detailed in Section 3.3.1) of the garnet sand layer will contribute resistance to heat transfer. The thermal resistance contributes to a reduction in the temperature of the rear polymer surface by 180°C and produces a 12 second time delay in attaining the maximum temperature at that surface relative to the front garnet sand surface. Collectively, the SEM imaging and temperature measurements indicate that decomposition of the GFRP samples during flame spraying is not occurring.

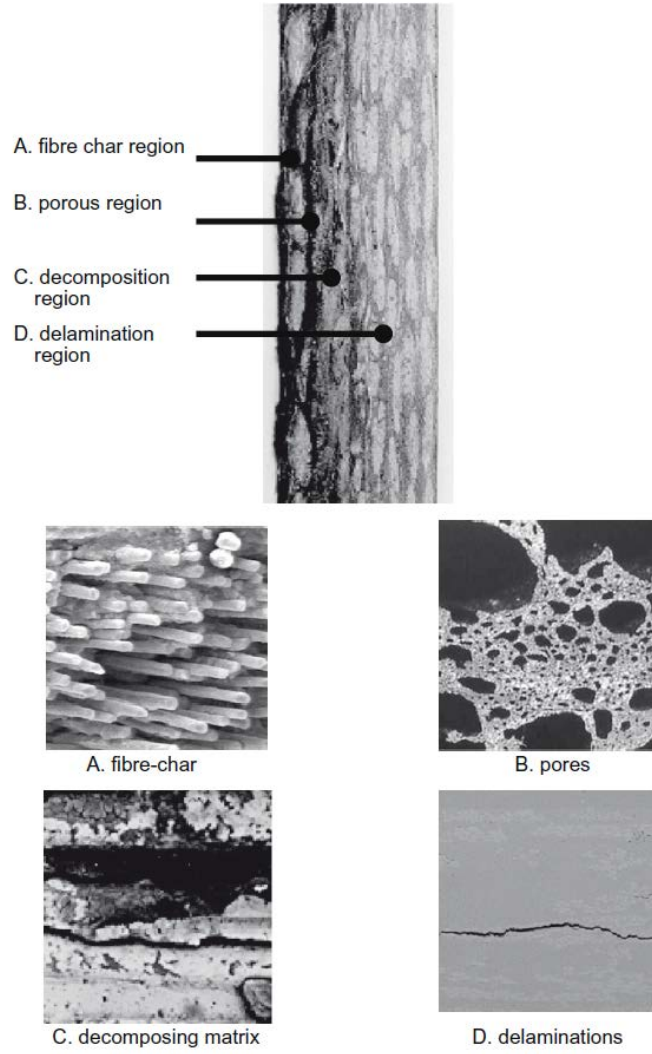


Figure 3.6: Cross-sectional view of fire-damaged GFRP [7]

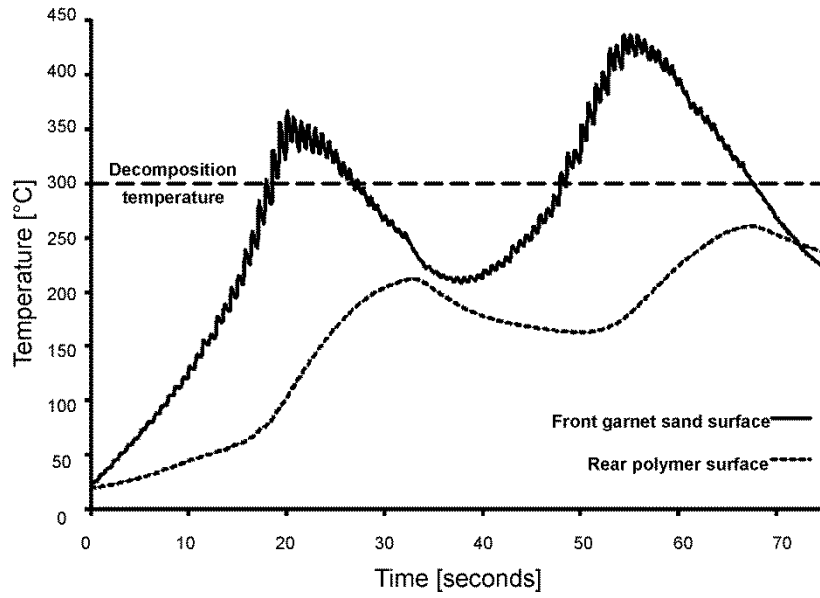


Figure 3.7: Temperature measurements along front garnet sand and rear polymer surfaces during flame spraying

3.3 Experimental Results

3.3.1 Insulated Tests

Temperature measurements at different locations on the metallic coating, polymer, and uncoated garnet sand surfaces were taken. Note that the thicknesses were approximately 0.34 mm for the coating (2 passes), 0.6 mm for the garnet sand and 1.2 mm for the polymer (2 layers) layers. Figures 3.8 and 3.9 show the variation of the temperatures along the coating and polymer surfaces of the coated sample. The standard error of the mean of the average surface temperatures ranged from 2.4°C at the heating wire to 0.3°C at a 100 mm distance away from the heating wire, for all surfaces. The transient temperature profiles of the control sample with garnet sand and polymer surfaces, were similar to the coated samples and are shown in Figs. 3.10 and 3.11.

From Figs. 3.8 to 3.11, it can be observed that the surface temperatures increased significantly near the heating wire. Far away from the wire, the transient surface temperature change was small. The surface temperature profiles of the top coating and garnet sand surfaces (Fig. 3.8 and 3.10) show higher temperatures close to the heating wire than that of the bottom uncoated polymer surfaces beneath it (Fig. 3.9 and 3.11). Beyond 20 mm from the heating wire, the surface temperatures were approximately equal for all the samples' surfaces. The uncoated samples temperatures are noticeably higher than the coated sample's temperatures less than 20 mm from the heating wire.

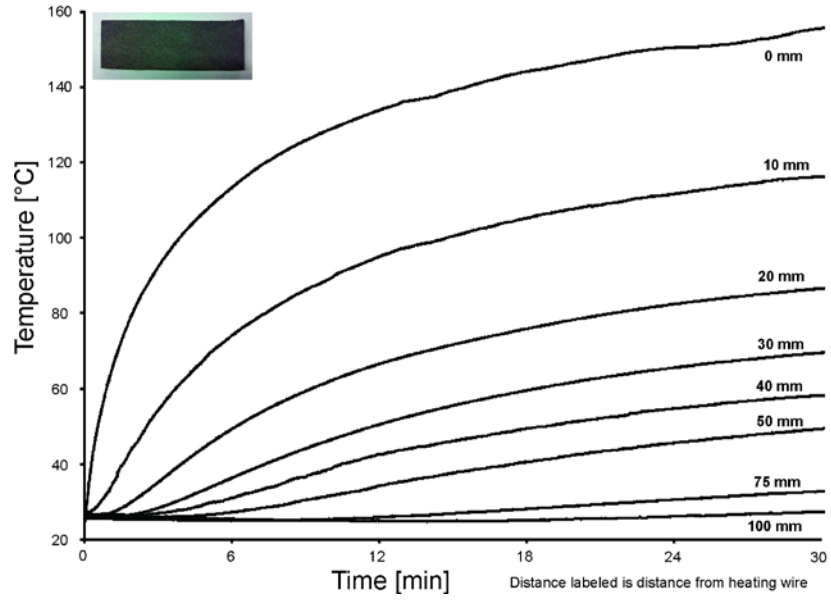


Figure 3.8: Transient temperature profile of coating surface

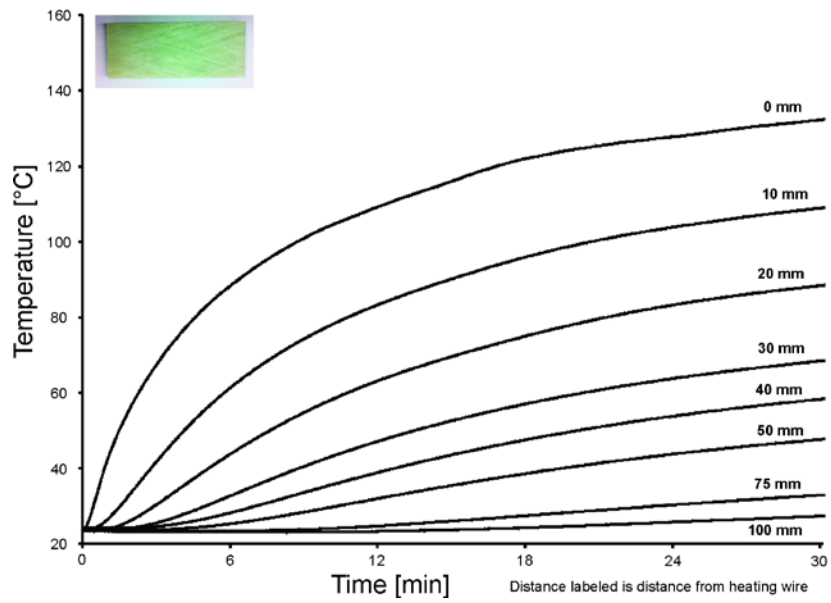


Figure 3.9: Transient temperature profile of polymer surface

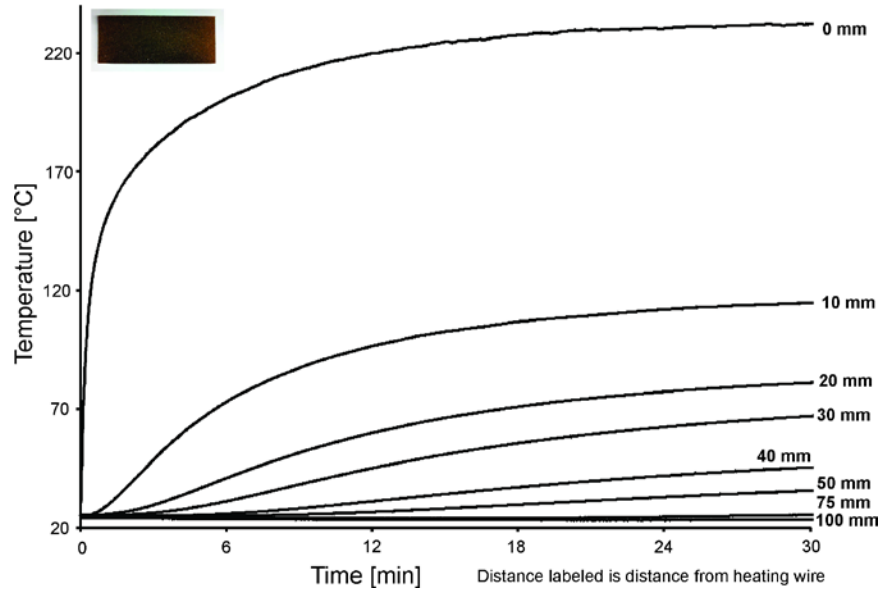


Figure 3.10: Transient temperature profile of garnet sand surface – Control

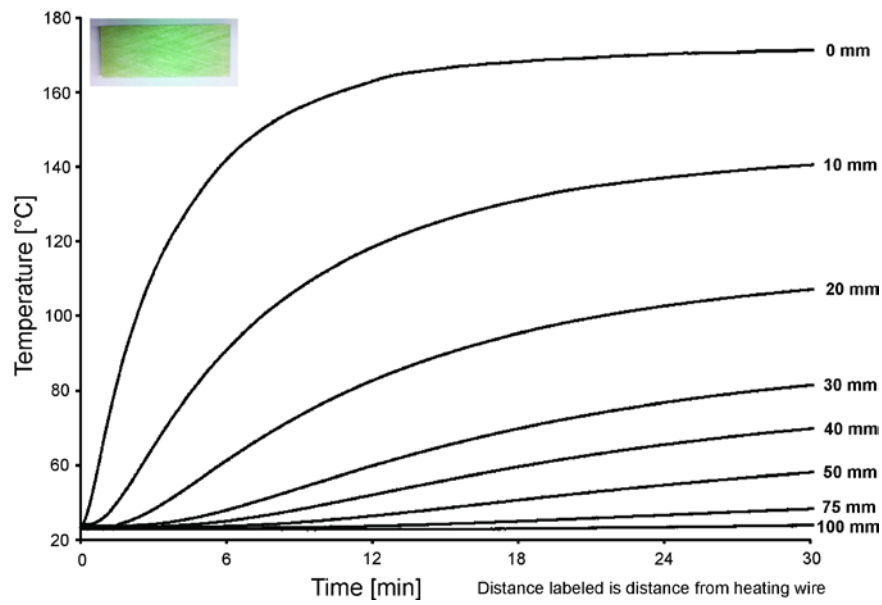


Figure 3.11: Transient temperature profile of polymer surface – Control

It should be noted that since both the top and bottom surfaces are insulated, the temperature continues to increase after 30 minutes. The heating power was maintained constant at 5.22 ± 0.01 W across the heating wire for both the coated and control sample tests. If there was perfect insulation, the temperature would increase continually. Steady state would be reached when the heat generated by the heating wire is equal to the heat lost both through the insulation and from the four thin sides of the samples. It is evident from Figs. 3.8 to 3.11 that the change in the values of the slopes of the temperature profiles are small beyond 20 minutes of heating, especially near the heating wire. Also the spatial temperature differences between the coated and control samples are significant after 30 minutes of heating.

The thermal conductivity of the coating was calculated in two steps. First, the composition of the powder (88 wt. % aluminum and 12 wt. %) was converted to volume percent to determine the metallic effective thermal conductivity as shown in the Eq. 3.1a. The total effective thermal conductivity of the coating was then calculated using a parallel path method for the metal components and assuming that the pores are filled with air as shown in Eq. 3.1b [5, 8]. Since the heat will not necessarily flow through each component (series resistive path), and will follow the path of least resistance, the parallel path method was chosen.

$$k_{\text{Metal}} = v_{\text{Al}}k_{\text{Al}} + v_{\text{Si}}k_{\text{Si}} \quad (3.1a)$$

$$k_{\text{C}} = v_{\text{Metal}}k_{\text{Metal}} + v_{\text{air}}k_{\text{air}} \quad (3.1b)$$

The volume fractions of the garnet sand and glass fiber to epoxy were determined from image analysis (see Table 3.1) and used to calculate the

equivalent thermal conductivities of these layers. It should be noted that the following assumptions apply to ideal fiber-reinforced composites [9]: (1) the composites are macroscopically homogenous, (2) the fibers and epoxy are homogenous and have constant thermal properties (isotropic), (3) the thermal contact resistance between the fiber and epoxy is negligible, (4) the composite is free of voids, (5) the problem is two dimensional (6) the fibers are arranged in a square periodic array (the fibers are uniformly distributed in the matrix), (7) the fibers are equal and uniform in shape and size. Based on the SEM images of the garnet sand and fiber in the epoxy matrix (see Fig. 3.2), it is reasonable to make the ideal fiber-reinforced composite assumptions. Again, the parallel path method will be used to calculate the effective thermal conductivity. The thermal conductivities of the raw materials are as follows:

Epoxy [10]: 0.21 W/m°C

Garnet sand [11]: 1.6 W/m°C

Glass fibers [12]: 1.3 W/m°C

It should be noted that the garnet sand and glass fiber-epoxy matrices will be treated as one polymer layer. This is justified due to the roughly equivalent thermal conductivities and that the polymer layer is much thicker than the garnet sand layer. For the thicker samples in Section 3.3.2 and 3.3.3, the garnet sand layer thickness is less than 10% of the polymer's thickness. This is further justified since it is the polymer surface temperature that is of interest and not a temperature in the cross-section. Nevertheless, it should be noted that the garnet sand layer is closer to the coating layer and

would thereby experience a greater temperature drop. The thermal conductivities are summarized in Table 3.2.

Table 3.2: Thermal conductivities of the layers

Layer	Thermal Conductivity
Coating	176 W/m°C
Garnet sand and epoxy	0.97 W/m°C
Glass fibers and epoxy	0.88 W/m°C

The higher temperatures of the coating surface were due to the high thermal conductivity of the aluminum-12silicon. The effective thermal conductivity of the garnet sand and glass fiber-reinforced epoxy polymer substrates is two orders of magnitude lower. The larger thermal conductivity of the metal coating promoted heat conduction, resulting in higher surface temperatures. Also, the thickness of the coating and substrate ensemble played a role in its temperature distribution.

It is well known that bodies with low cross-sectional thicknesses are likely to possess a uniform temperature across the cross-section [8]. If the Biot number,

$$\text{Bi} = \frac{hL_c}{k} \quad (3.2)$$

which is defined as the product of the heat transfer coefficient, h , and characteristic length of the body, L_c , divided by the material thermal conductivity, k , is much less than 1, the temperature of the coating-substrate ensemble will not vary across the cross-section and will vary only along the length of the plate. In this portion of the study, the samples were completely insulated. Therefore, $h = 0$ and thus $\text{Bi} = 0$, which supports the observed uniform temperatures in Figs. 3.8 to 3.11 along the samples at distances beyond 20-mm.

Again, the objective of the deposition of a metal coating onto the polymer-based substrate samples is to minimize hot spots and increase the surface temperature distribution away from the heating wire. Figure 3.12 shows the spatial temperature distribution after 5 minutes of heating on the surfaces of the coating and uncoated garnet sand (control) each on a flat

polymer plate. The surface temperature of both surfaces decayed uniformly from the heating wire. There was a “cross-over point” where the temperatures of the coated and control samples were equal. For the coated and garnet sand surfaces, this point was constant with respect to time, occurring at approximately 10 mm from the heating wire. Beyond this point, the coating surface temperatures were higher than that of the control samples due to rapid heat conduction through the coating.

Similar increases in surface temperature were also observed for the polymer surfaces on the rear side of the sprayed samples (Fig. 3.13). Figure 3.13 shows that the spatial surface temperature of the polymer surface decayed uniformly from the heating wire and that the “cross-over point” on the polymer surfaces was also constant and independent of time at about 20 mm from the heating wire. The lower maximum temperature ($\sim 83^{\circ}\text{C}$) of the polymer surface compared to the coating surface ($\sim 115^{\circ}\text{C}$) was likely due to the lower thermal conductivity of polymer structures.

The impact of the high thermal conductivity metal coating is evident from the temperature variations between the coated samples and the uncoated garnet sand (control) samples. The spatial surface temperature distributions after 10 and 30 minutes of heating are shown in Figs. 3.14 to 3.17 for all surfaces. The slopes of the temperature profile curves of the coating and uncoated control surfaces did not change significantly, resulting in the cross-over point occurring at approximately 10-mm and 20-mm from the heating wire along the top (coating/garnet sand) and bottom (polymer) surfaces, respectively. However, for time periods shorter than 5 minutes the temperature that characterized the “cross-over point” decreased, due to the

lower transient temperatures (see Figs. 3.8 and 3.9). It should be noted that the garnet sand temperature at the heating wire was much higher than all other measured temperatures and was excluded from Figs. 3.12, 3.14 and 3.16 such that the spatial trends were more evident. The temperatures at the heating wire along the garnet sand surface after 5, 10 and 30 minutes of heating were 195°C, 215°C, and 232°C, respectively.

Far from the heating wire, the top (coating side) and rear (uncoated polymer side) surface temperatures of the coated samples are consistently higher than those of the uncoated control samples. For example, after only 5 minutes of heating, there is a noticeable increase in temperature up to 50 mm from the heating (see Figs. 3.12 and 3.13). After 10 minutes of heating, the temperature increase is roughly 5°C 50-mm from the heating wire along both the top and bottom surfaces (see Figs. 3.14 and 3.15). Figures 3.16 and 3.17 show that the surface temperatures of the coating and polymer sides of the sprayed samples at 50-mm from the heating wire are 14°C and 10°C higher than the uncoated control sample, respectively. This is significant and demonstrates that the coating provides an effective medium of heat transfer in metallic coating-polymer composite structures.

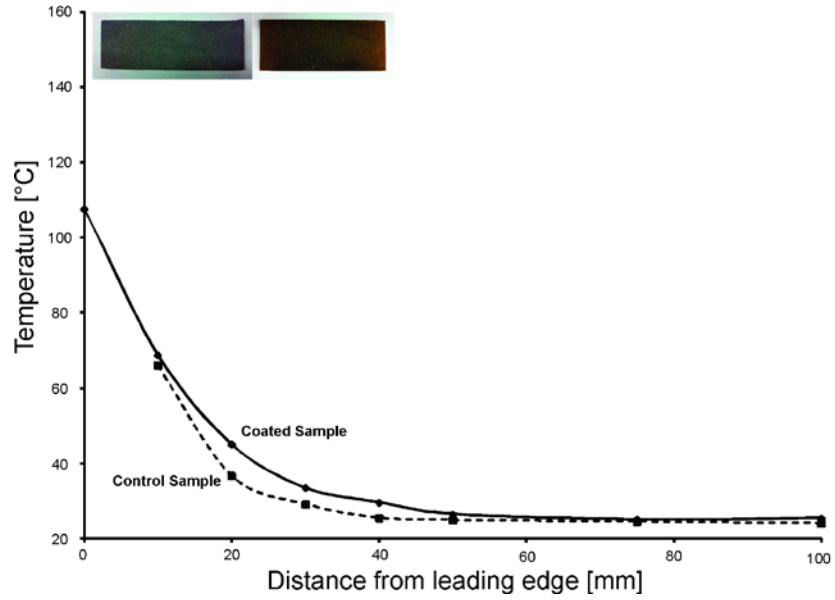


Figure 3.12: Spatial temperature profiles of the coating and uncoated garnet sand (control) surfaces after 5 minutes of heating (insulated tests)

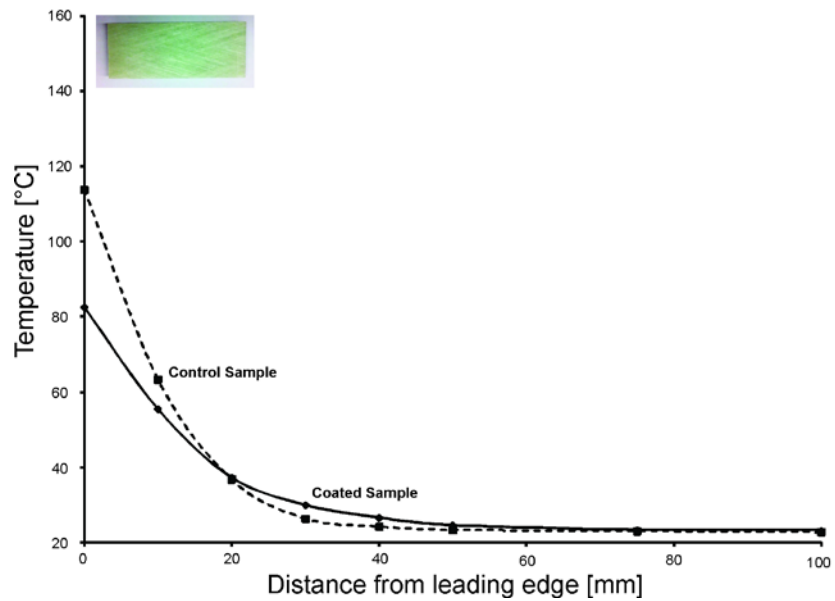


Figure 3.13: Spatial temperature profiles of the rear polymer (coating and control) surfaces after 5 minutes of heating (insulated tests)

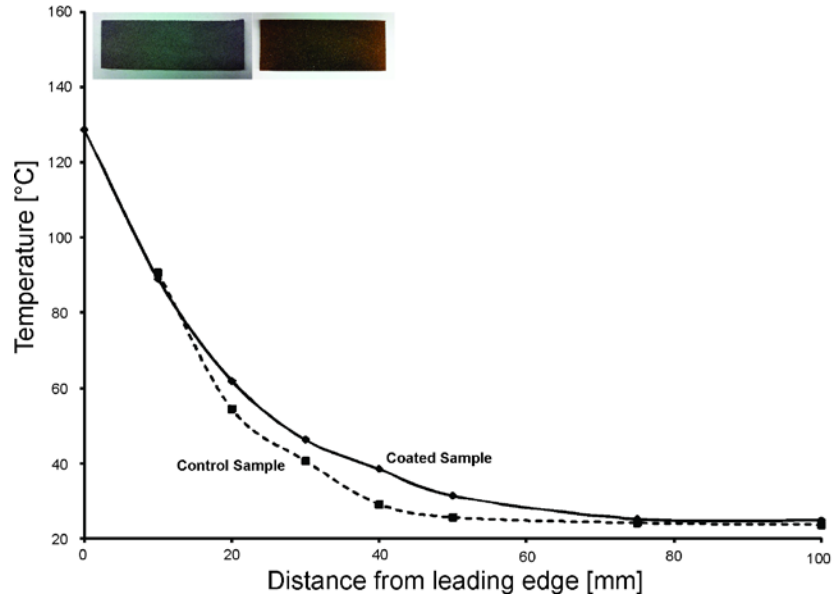


Figure 3.14: Spatial temperature profiles of the coating and uncoated garnet sand (control) surfaces after 10 minutes of heating (insulated tests)

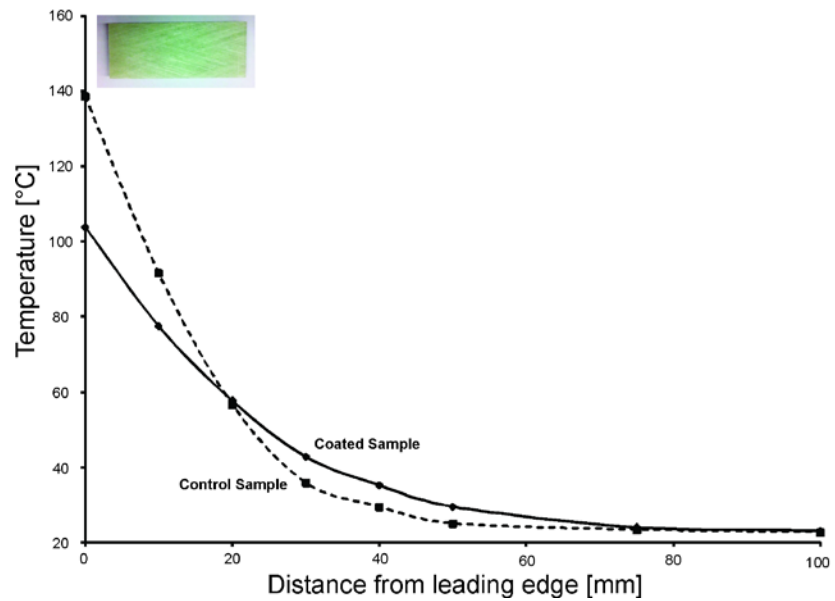


Figure 3.15: Spatial temperature profiles of the rear polymer (coating and control) surfaces after 10 minutes of heating (insulated tests)

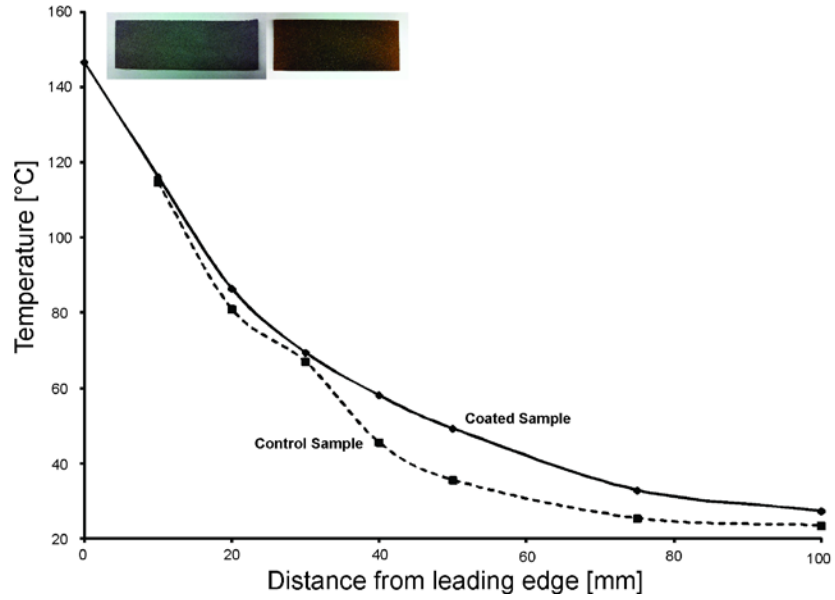


Figure 3.16: Spatial temperature profiles of the coating and uncoated garnet sand (control) surfaces after 30 minutes of heating (insulated tests)

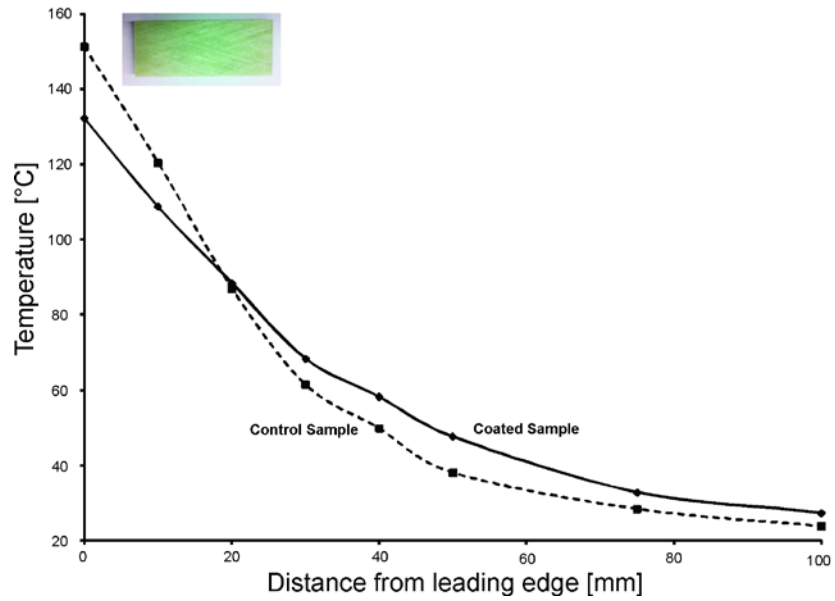


Figure 3.17: Spatial temperature profiles of the rear polymer (coating and control) surfaces after 30 minutes of heating (insulated tests)

3.3.2 Wind Tunnel – Test #1 with Coating Exposed

Since the coating improved heat transfer of the insulated metallic coating-polymer composite flat plates, this concept was investigated further. Thicker polymer samples were fabricated, following a similar fabrication procedure, but with eight layers versus the previous two layers. The thicker polymer (9.2 mm) allowed for more variation between the coating and polymer surface temperatures. Also, the thicker polymer is more representative of what is commonly fabricated in the aerospace [13] and wind turbine [14] industries. The samples were exposed to forced convection in a high speed wind tunnel. The measured wind speed was 27.8 ± 0.1 m/s. The power was controlled to obtain a steady state coating surface temperature of $223.0 \pm 2.3^\circ\text{C}$ at the heating wire, requiring a power input of 88.0 ± 0.1 W across the heating wire. Similarly to the insulated samples, control samples without a coating were prepared to compare the surface temperatures of coated and non-coated polymers.

Temperature measurements along the metallic coating, polymer and uncoated garnet sand surfaces were recorded. The transient temperature profile along the coating and polymer surfaces of the coated sample is shown in Figs. 3.18 and 3.19, respectively. For all surfaces, the standard error of the mean of the average surface temperatures was highest at the heating wire at 2.9°C due to the highest temperatures occurring here. Thereafter, it decreased from 0.9°C at a 10 mm, to 0.1°C at a 100-mm distance away from the heating wire. Again, the transient temperature profiles of the control

sample with garnet sand and polymer surfaces were similar to those shown in Figs. 3.18 and 3.19, though there was less spatial temperature variation.

From Figs. 3.18 and 3.19, it can be seen that the surface temperatures increased near the heating wire. The temperature change away from the heating wire was much less significant. The coating temperatures profile (see Fig. 3.18) is similar to those observed for the insulated test (see Fig. 3.8), however, with higher temperatures and on a shorter time scale. The higher temperatures can be explained by the larger power input through the heating wire, which was required to overcome the reduction in temperature caused by forced heat convection.

The polymer surface temperature profile (see Fig. 3.19) is similar to the coating profile, albeit with much lower temperatures and a significant time delay. There is much less resistance for heat conduction through the coating compared to the thick polymer layer, resulting in the time delay and lower temperatures. Due to convection, the Biot number will not be zero as in the insulated tests (see Eq. 3.2). A similar explanation as the insulated tests can be used to justify the lower polymer surface temperature.

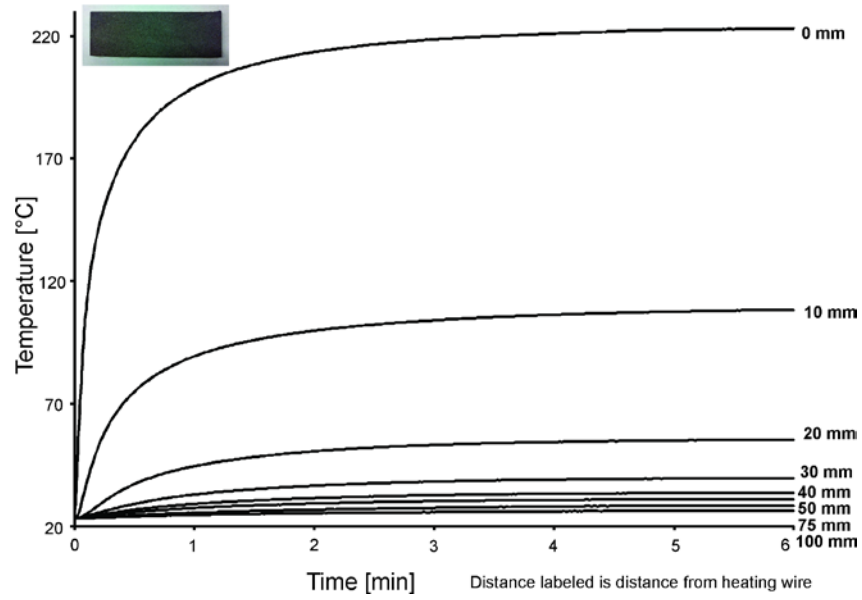


Figure 3.18: Transient temperature profile of coating surface for air flow at
27.8 m/s

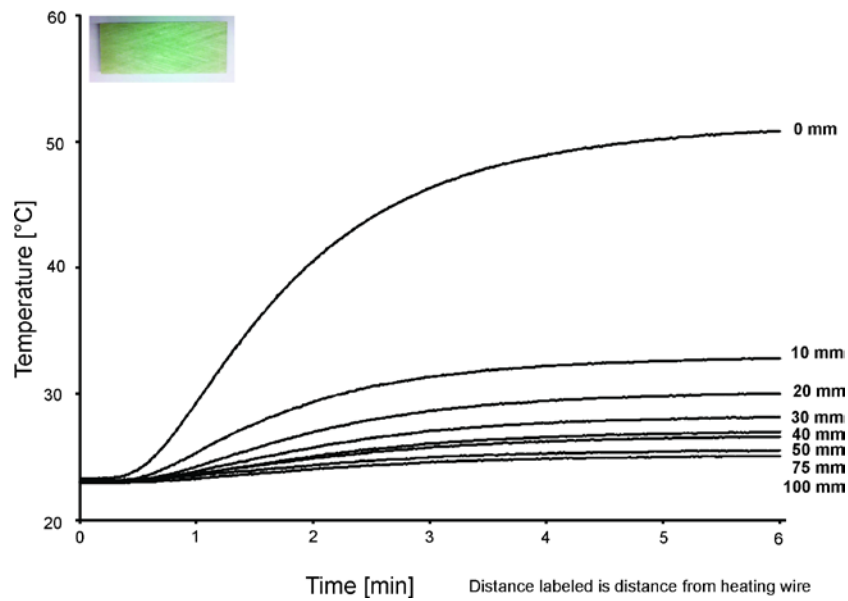


Figure 3.19: Transient temperature profile of polymer surface for air flow at
27.8 m/s

Recall that if the Biot number (see Eq. 3.2) of a layer is much less than 1, the temperature across the cross section will not vary. Using layer thicknesses, thermal conductivities and the respective heat convection coefficients (see Section 3.3.2), the Biot numbers for the coating and polymer layers are 2.4×10^{-4} and 0.67, respectively.

$$\text{Bi}_C = \frac{h_C t_C}{k_C} = \frac{127.1 \text{ W/m}^2 \cdot \text{°C} * 0.00034 \text{ m}}{176 \text{ W/m} \cdot \text{°C}} = 2.4 \times 10^{-4} \quad (3.3a)$$

$$\text{Bi}_P = \frac{h_P t_P}{k_P} = \frac{64.5 \text{ W/m}^2 \cdot \text{°C} * 0.0092 \text{ m}}{0.88 \text{ W/m} \cdot \text{°C}} = 0.67 \quad (3.3b)$$

Since the coating's Biot number is much less than 1, the temperature variation across the cross section coating is consistent. Conversely, the polymer's Biot number of approximately 1 indicates that there is temperature variation across the polymer's cross section. This effect can be largely attributed to the differences in thicknesses and material thermal conductivities, as shown in the Biot number calculations (see Eqs. 3.3a and 3.3b).

For the control experiment, the heating power was continually set to $46.0 \pm 0.1 \text{ W}$ while the air velocity maintained at $27.6 \pm 0.1 \text{ m/s}$. The power was reduced such that the steady state temperature at the heating wire ($244.7 \pm 2.9\text{°C}$) was approximately the same as the coated sample's experiment ($223.0 \pm 2.3\text{°C}$). The transient temperature profile along the coating surface is shown in Fig. 3.20. Since the temperature at the heating wire is much greater than all other temperatures, Fig. 3.21 has been included

to show the trends beyond the heating wire. The transient temperature profile of the polymer surface of the control sample is shown in Fig. 3.22.

Identical to the coated sample, the surface temperatures decayed uniformly from the heating wire as shown in Figs. 3.20 to 3.22. Along the garnet sand surface, 10 mm from the heating wire the temperature was roughly 42°C. At distances 20 mm and greater, the temperature increase was at most 5°C indicating that the garnet sand does not conduct heat effectively (see Fig. 3.21). While the highest temperature ($244.7 \pm 2.9^\circ\text{C}$) was at the heating wire, the next highest temperature was 50°C at the leading edge along the polymer surface. While the temperature 10 mm from the leading edge was 30°C, beyond this distance there was almost no heating observed along the uncoated sample's polymer surface (see Fig. 3.22).

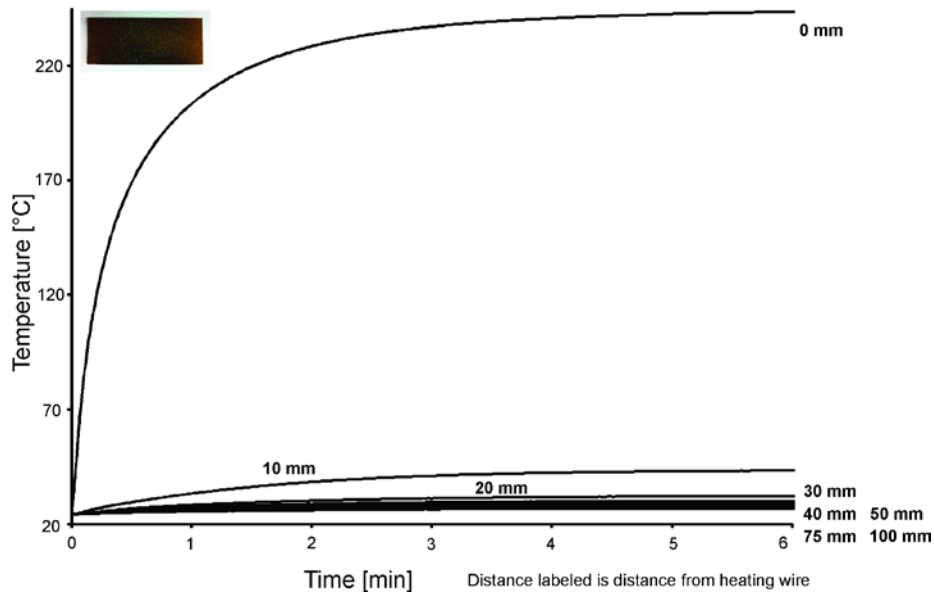


Figure 3.20: Transient temperature profile of garnet sand for airflow at 27.6 m/s (at heating wire) – Control

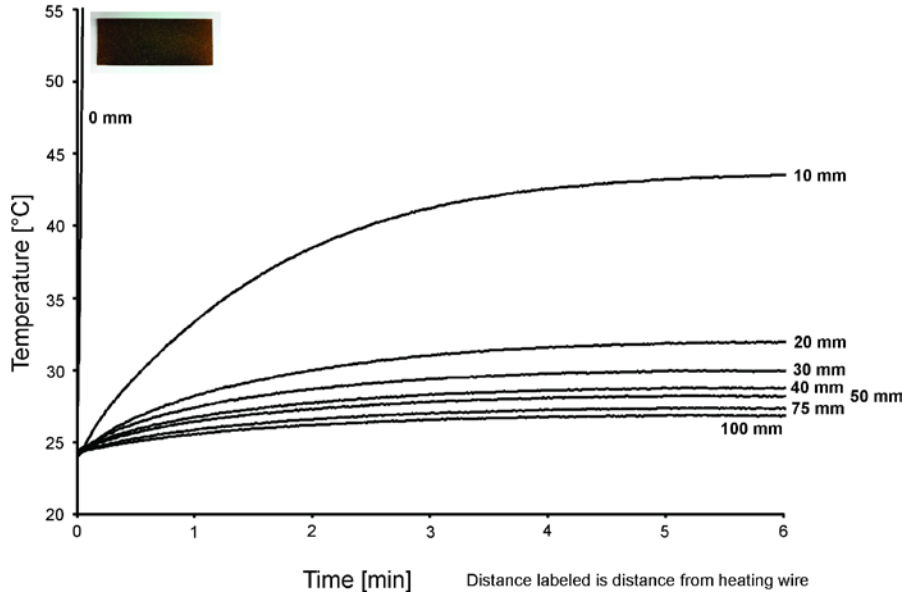


Figure 3.21: Transient temperature profile of garnet sand for airflow at 27.6 m/s (away from heating wire) – Control

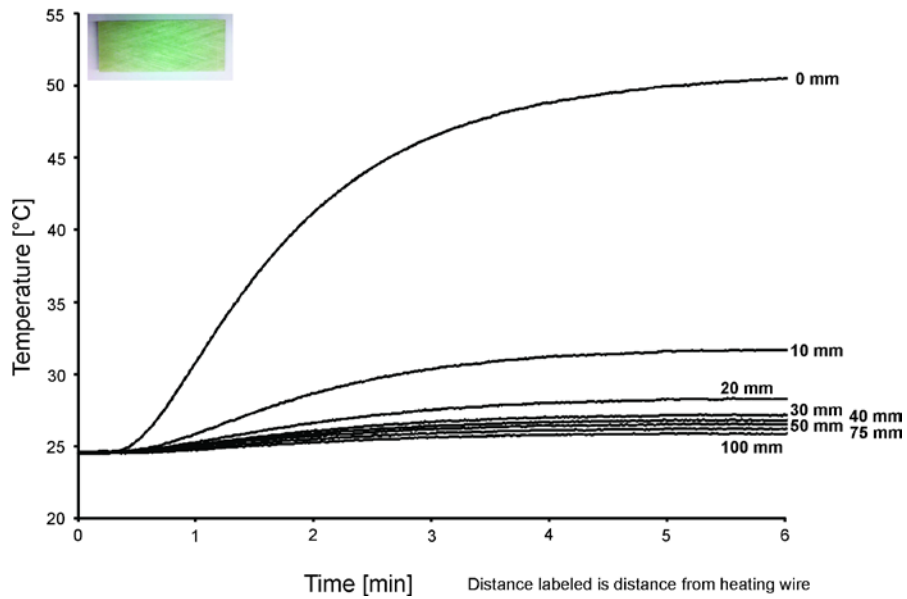


Figure 3.22: Transient temperature profile of polymer surface for airflow at 27.6 m/s – Control

Figures 3.23 and 3.24 show the temperature difference between the coating sample surfaces and the control surfaces ($T_C - T_{\text{Sand}}$). From the coating and garnet sand surface temperatures, it is obvious that the coating is effective at conducting the heat away from the heating wire. All the temperatures of the coated sample are greater than that of the control sample, except at the heating wire. At a distance of 10 mm from the heating wire, the temperature of the coating sample is roughly 60°C higher, while the temperature of the control samples was 20°C higher at the heating wire. Further, the temperature difference 20 mm from the heating wire is 20°C. Therefore, to achieve a temperature increase of at least 20°C on a polymer structure, heating wires would need to be placed every 40 mm along a coated surface. At large distances away from the heating wire the coating surface's temperature increase was less significant.

Along the polymer surfaces, the surface that was associated with the coating sample had higher surface temperatures than that which was associated with the control sample (see Fig. 3.24). This temperature difference was higher near the heating wire. However, this temperature difference of up to 3°C was insignificant compared to the temperature difference between the coating and garnet sand surfaces. With a much lower thermal conductivity, the polymer resists heat conduction both in the axial and transverse direction. Although the thin coating layer conducts well axially and transversely, much more heat can be conducted axially (lengthwise along the sample), resulting in the higher measured coating surface temperatures versus the garnet sand surface.

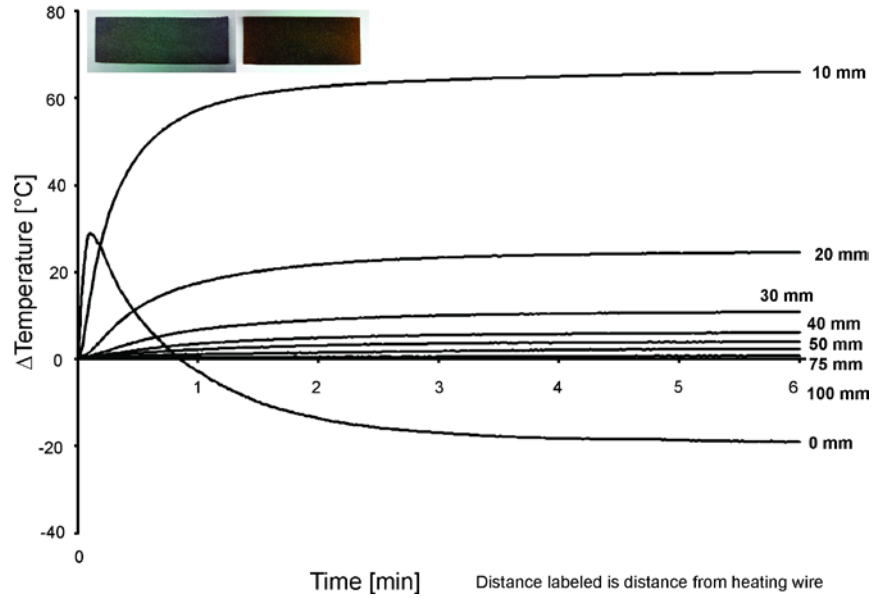


Figure 3.23: Transient temperature difference between the coating and garnet sand (control) surfaces ($T_C - T_{\text{Sand}}$)

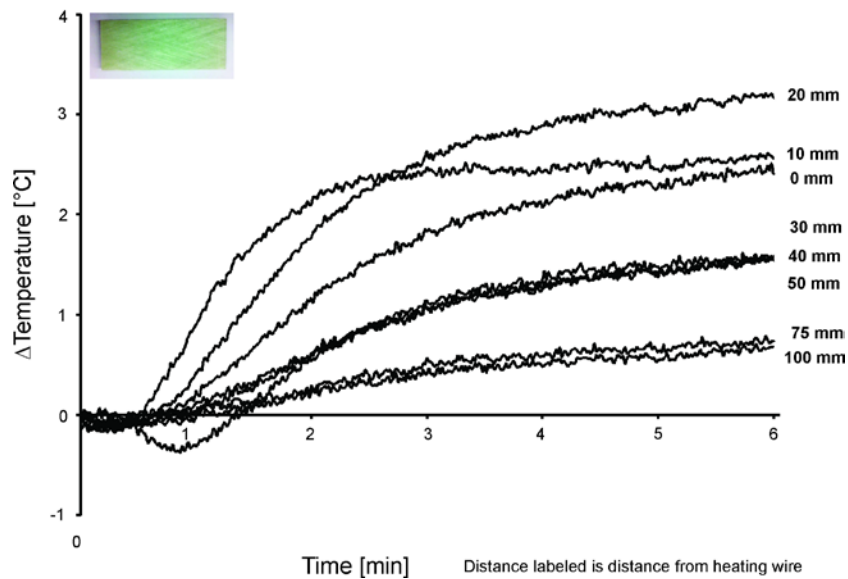


Figure 3.24: Transient temperature difference of the rear polymer (coating and control) surfaces ($T_C - T_{\text{Sand}}$)

The spatial temperature profile of the coating and polymer surfaces after 6 minutes of heating are shown in Fig. 3.25. From this figure, it is obvious that the polymer surface temperature is much less than the coating surface temperature. Far away from the heating wire, the temperatures of the surface coalesce as they approach the ambient temperature. This wind tunnel test with the coating exposed has revealed that the coating is effective at conducting heat along the surface of a thick polymer (see Fig. 3.23), without a significant increase along the polymer surface (see Fig. 3.24).

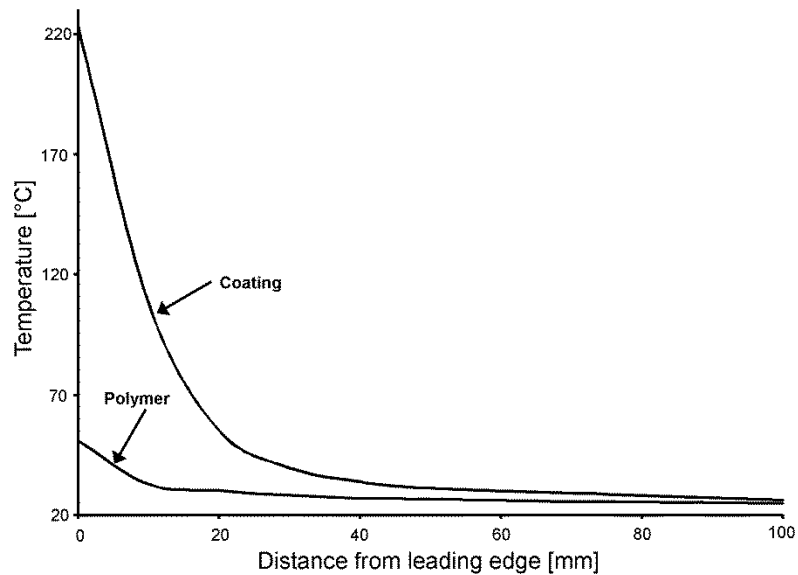


Figure 3.25: Spatial temperature profile of the coating and polymer surfaces after 6 minutes of heating

In this test, steady state was reached after approximately six minutes as can be observed in Figs. 3.18 to 3.22. The Fourier number has the physical significance of the ratio of heat conducted through a body to the heat stored in the body. Therefore a large Fourier number represents faster conduction of heat through the body [5]. The Fourier number is defined in Eq. 3.4. Although the thermal diffusivity of aluminum ($9.7 \times 10^{-5} \text{ m}^2/\text{s}$) and polymers are very small ($6.7 \times 10^{-8} \text{ m}^2/\text{s}$), the thickness squared is also small (coating $1.2 \times 10^{-7} \text{ m}^2$; polymer $8.5 \times 10^{-5} \text{ m}^2$), meaning steady state will likely be reached on the order of minutes [5, 15].

$$\text{Fo} = \frac{at}{L_c^2} \quad (3.4)$$

3.3.3 Wind Tunnel – Test #2 with Top Polymer Layer

Although the first wind tunnel test revealed that the coating was effective at conducting heat, this test left the coating open to ambient conditions, without any oxidation or erosion protection. Therefore, a second wind tunnel experiment with a thin polymer layer (0.9 mm) wound above the coating was performed. From the original insulated tests, it is known that a thin polymer layer could conduct heat without a large temperature drop. With a single pass of glass fibers wound axially around the samples following flame spraying, temperature measurements of both top and bottom polymer surfaces were obtained. Also, thermocouples that were attached to the coating, between the coating and top polymer surfaces, were used to measure the temperature of the embedded coating.

The measured wind speed was 26.5 ± 0.1 m/s while the power was carefully controlled to not denature the top polymer layer. This was important since the heating wire was also embedded below this layer, and there was no coating above the heating wire to conduct away the heat. The power input was lower than previous tests at 31.41 ± 0.06 W.

Figures 3.26 to 3.28 show the transient temperature profiles along the coating, top polymer, and bottom polymer surfaces, respectively. For all surfaces, the largest standard error of the mean of the average surface temperatures was highest at the heating wire at 3.0°C . Thereafter, it decreased from 0.6°C at 10 mm, to 0.1°C at 75 mm away from the heating wire.

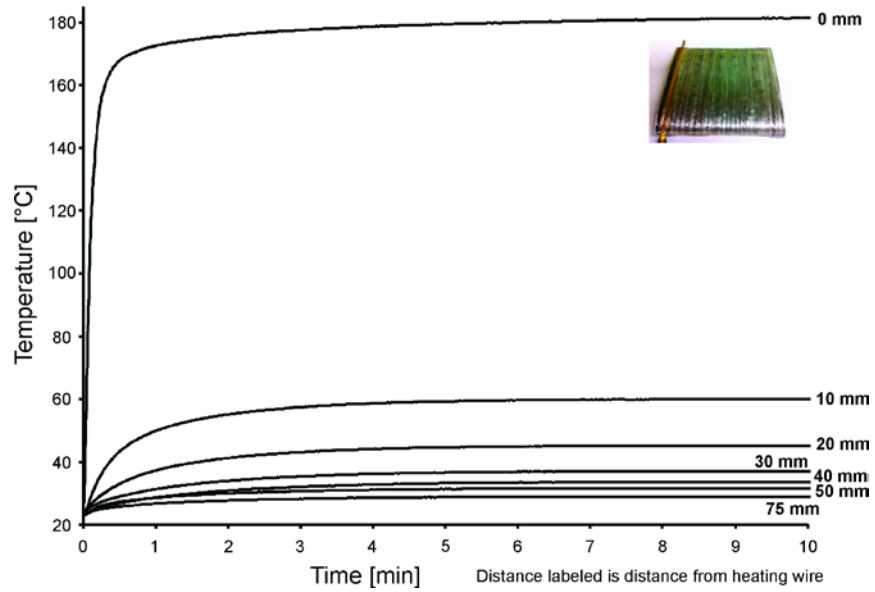


Figure 3.26: Transient temperature profile of the coating (layer thickness = 0.51 mm)

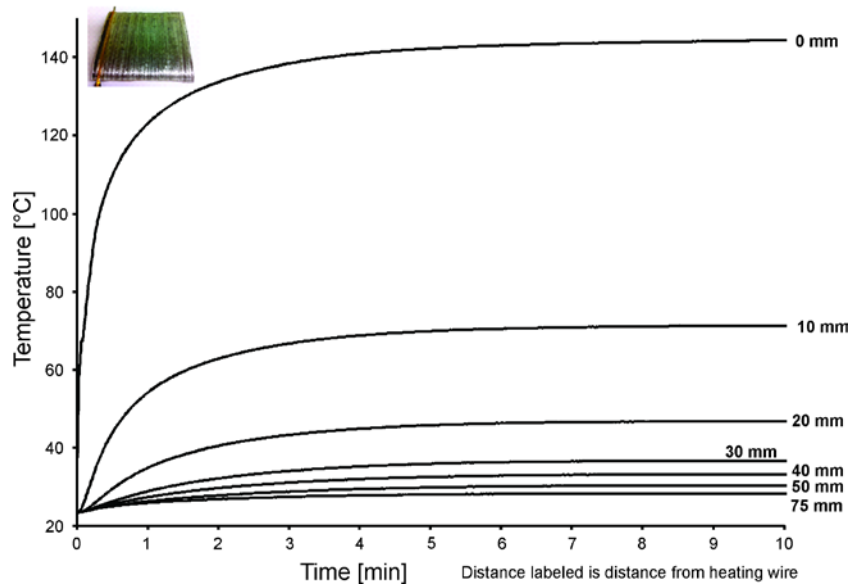
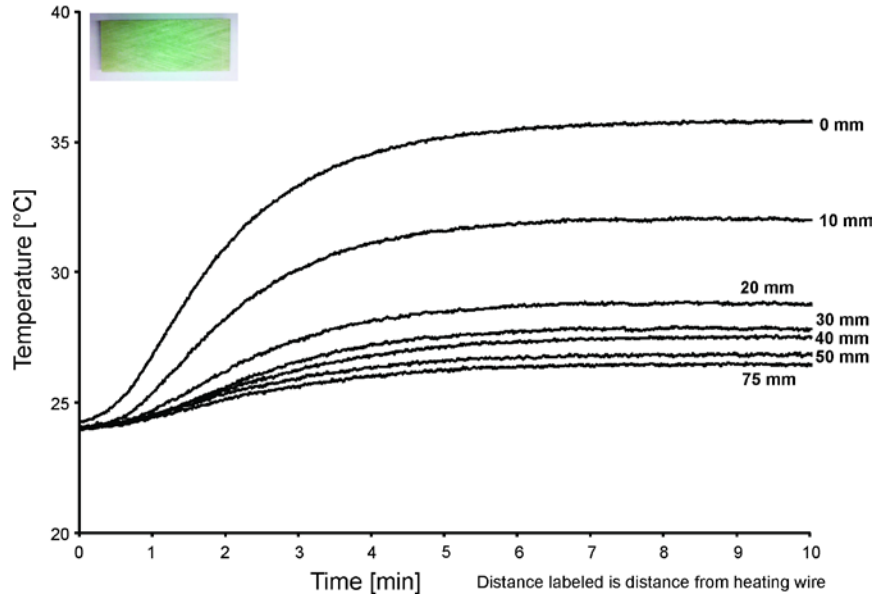


Figure 3.27: Transient temperature profile of the top polymer surface (layer thickness = 0.9 mm)



**Figure 3.28: Transient temperature profile of the bottom polymer surface
(layer thickness = 9.2 mm)**

From Figs. 3.26 to 3.28, it can be seen that the highest temperatures were obtained near the heating wire. Away from the heating wire, the temperature increase was much less significant. The trends of the coating and top polymer surface temperatures (see Figs. 3.26 and 3.27) were similar to the profile of the coating from the first wind tunnel test (see Fig. 3.18). However, the temperatures recorded along the coating and top polymer surfaces are lower than the temperatures of the coating surfaces during the first wind tunnel test, in which the coating surface was open to the flowing ambient fluid. This can be attributed to the lower power input (31.41 ± 0.06 W vs. 88.0 ± 0.1 W) at the heating wire. The steady state temperature difference 10 mm from the heating wire between the first (108°C) and second (60°C) wind tunnel tests is roughly 50°C . This lower power input also resulted

in significantly lower temperatures at the heating wire along the bottom polymer surface (50°C vs. 35°C), reducing the hottest location along this surface.

The bottom polymer temperature profile (see Fig. 3.28) is similar to the polymer temperature profile of the first wind tunnel test (see Fig. 3.19). In the second wind tunnel test the temperature at the heating wire is reduced, thereby reducing the spatial temperature variation along the bottom surface. This is important as the inner surface of a polymer structure could be exposed to flammable substances [16]. For example, for airfoils, the flash point of common jet fuels is approximately 50°C at atmospheric pressures [17]. However, for safety the autoignition temperature is more relevant since it is the lowest temperature at which a substance can spontaneously ignite and these temperatures are much lower than this limit [18]. For jet fuel, the autoignition temperature is much higher than our maximum temperature of 180°C at the heating wire [19].

The coating and top polymer surface temperatures appear to have levelled out after 3 minutes, with only slight increases in temperature thereafter (see Figs. 3.26 and 3.27). Reaching steady state after a short period of time is expected due to the thermal diffusivities of the coating and polymer layers in the Fourier number (see Eq. 3.4). However, the slight increases can be attributed to heat conduction resistance through the top polymer layer due to the much lower thermal conductivity.

Although the coating conducts heat effectively, as evidenced by the Biot number in the first wind tunnel test (see Eq. 3.3a), it cannot conduct

more heat than the top and bottom polymer layers combined (similar to series resistive path method). Due to the large thickness of the bottom layer, most of the heat will be conducted through the top polymer layer. The Biot number of the top polymer layer is much less than 1, indicating that the temperature across the thickness is uniform.

$$\text{Bi}_P = \frac{h_P t_P}{k_P} = \frac{63.1 \frac{\text{W}}{\text{m}^2 \cdot ^\circ\text{C}} * 0.0009 \text{ m}}{0.88 \frac{\text{W}}{\text{m} \cdot ^\circ\text{C}}} = 0.065 \quad (3.5)$$

However, the Biot number of the top polymer layer is still much greater than that of the coating in the first wind tunnel test (2.4×10^{-4}) resulting in a greater resistance to heat transfer throughout the ensemble. The slightly different trends between the two wind tunnel tests coating temperature profiles (see Figs. 3.26 and 3.18) can be attributed to the difference in Biot numbers on the top surfaces. In both cases, this surface was nearest to the heating wire while convecting to the ambient fluid since it was designed to be the outer most surface of the structure.

It should be noted that the time scales of the first and second wind tunnel tests were 6 and 10 minutes, respectively. The second wind tunnel test was extended past 6 minutes to reinforce that steady state has been reached; there are very slight temperature increases at the heating wire thereafter. Though the insulated tests were performed over a 30 minute period there was no convection to remove the heat from the samples, thereby requiring a significant amount of time to reach steady state. The fact that the second wind tunnel experiment with the embedded coating has reached steady state after 3 minutes indicates that the polymer-coating-polymer composite is

effective at rapidly conducting heat. This thin top polymer layer provides structural integrity and protection to the coating, while not significantly restricting heat transfer, such that de-icing will occur.

The steady state spatial temperatures of the coating, top polymer and bottom polymer are shown in Fig. 3.29. The temperature differences between all surfaces decrease from the heating wire. There is a large temperature difference between the coating and bottom polymer surfaces near the heating wire. The temperature difference between the coating and top polymer surfaces is roughly 30°C at the heating wire but decreases rapidly to only 5°C 30 mm from the heating wire. From Fig. 3.29, it is evident that the coating has significantly heated the top polymer surface, while not significantly heating the bottom polymer surface.

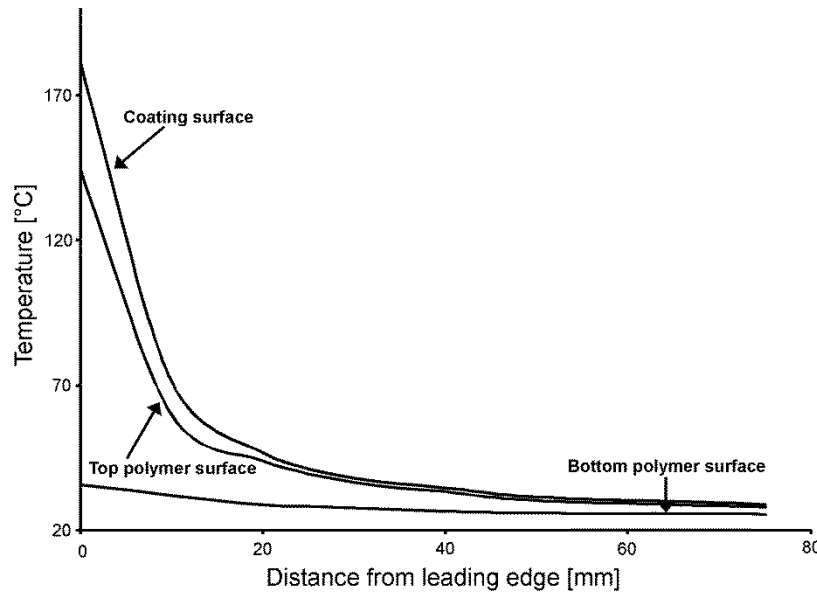


Figure 3.29: Spatial temperature profiles of coating, top and bottom polymer surfaces

Between the insulated, first and second wind tunnel tests some reoccurring trends were observed. In all tests, the surface temperatures decayed from the heating wire, along all surfaces. Also, the coating temperatures were consistently higher than the polymer surface temperatures. Table 3.3 has been prepared to summarize the relevant parameters mentioned earlier of all three test scenarios.

Table 3.3: Summary of experimental parameters

Test name	Power [W]	Wind Speed [m/s]	Heating Wire Steady State Temperature [°C]
Insulated Test	5.22 ± 0.01	N/A	111.1 ± 2.4
Insulated Test – Control	5.21 ± 0.01	N/A	215.3 ± 2.1 **
Wind Tunnel Test #1	88.0 ± 0.1	27.8 ± 0.1	223.0 ± 2.3
Wind Tunnel Test #1 - Control	46.0 ± 0.1	27.6 ± 0.1	244.8 ± 2.9 **
Wind Tunnel Test #2	31.41 ± 0.06	26.5 ± 0.1	181.4 ± 3.0

** Indicates that the heating wire surface is garnet sand and not the metallic coating, which applies to the other tests.

3.4 Analytical Model

3.4.1 Governing Equation and Assumptions

A mathematical model was developed to predict both the top and bottom polymer surface temperatures of both the wind tunnel tests. Regardless of the solution methodology, each solution begins with the general partial differential heat conduction equation. For a Cartesian coordinate system, the heat conduction equation is:

$$\frac{\partial}{\partial x} \left(k \frac{\partial T}{\partial x} \right) + \frac{\partial}{\partial y} \left(k \frac{\partial T}{\partial y} \right) + \frac{\partial}{\partial z} \left(k \frac{\partial T}{\partial z} \right) + q''' = \rho C_p \left(\frac{\partial T}{\partial t} \right) \quad (3.6)$$

Equation 3.6 can be simplified by assuming constant thermal properties (k , ρ , C_p) and no internal energy generation (q''') to Eq. 3.7:

$$\frac{\partial^2 T}{\partial x^2} + \frac{\partial^2 T}{\partial y^2} + \frac{\partial^2 T}{\partial z^2} = \frac{\rho C_p}{k} \left(\frac{\partial T}{\partial t} \right) \quad (3.7)$$

The general three-dimensional transient heat conduction problem can be solved using the separation of variables method. With this method, a temperature distribution for each layer can be obtained, and the constants can be obtained from the boundary conditions using the orthogonal expansion technique. However, the experimental results show that within 3 minutes, the temperature profiles of the polymer surfaces have achieved steady state. Further, using the Heisler charts for our Biot number ($Bi \approx 1$) of the bottom polymer surfaces to determine the Fourier number, and thereby the minimum amount of time to reach steady state, we conclude that steady state should be reached on the order of minutes [20]. Also, since some potential

applications include de-icing for airfoils, the transient response is not of interest [21]. Therefore it is assumed that there is a negligible temperature change with respect to time, noting that this assumption will neglect the initial transients. Given that both the right and left edges of our samples were insulated in the wind tunnel, and that the heating extended over the entire width of the sample, there is symmetry along the width of the samples. Further, since the thickest portion, the 0.9 cm layer, made up of polymer (0.7 cm) and garnet sand (0.2 cm), was much less than the 10 cm length of the sample, it is assumed that the heat conduction along the length of the sample is not as significant as on the heat conduction across the thickness of the sample. This assumption has been proven accurate for airfoils in which the thickness is less than 10% of the length [22].

Therefore, based on the symmetry along the width, and the ratio of thickness to length of the samples, the governing steady state equation can be simplified to one spatial dimension. Defining the y -coordinate as the thickness of the sample as shown in Fig. 3.30, the one-dimensional steady state governing equation for the temperature distribution in the samples is given by Eq. 3.8:

$$\frac{d^2T}{dy^2} \approx 0, \quad 0 < y < d \quad (3.8)$$

The boundary conditions for the one-dimensional model are (Eq. 3.9) as indicated in Fig. 3.31 for both the top and bottom polymer samples:

$$T_{(y=0)} = T_i \quad (3.9a)$$

$$-k \frac{\partial T_{(y=d)}}{\partial y} = h(T_{(y=d)} - T_{\infty}) \quad (3.9b)$$

Note that the surface temperature at $y = 0$ was experimentally determined. Further, note that the radiation effects are neglected since the experimental surface temperatures were relatively low. The solution to the governing equation is shown in Eq. 3.10; where the constants are determined from the boundary conditions. This solution will be applied along the polymer surface of the samples where the T_i values are known from Figs. 3.25 and 3.29:

$$T_{(y)} = \frac{h(T_i - T_{\infty})}{k + hd} y + T_{\infty} \quad (3.10)$$

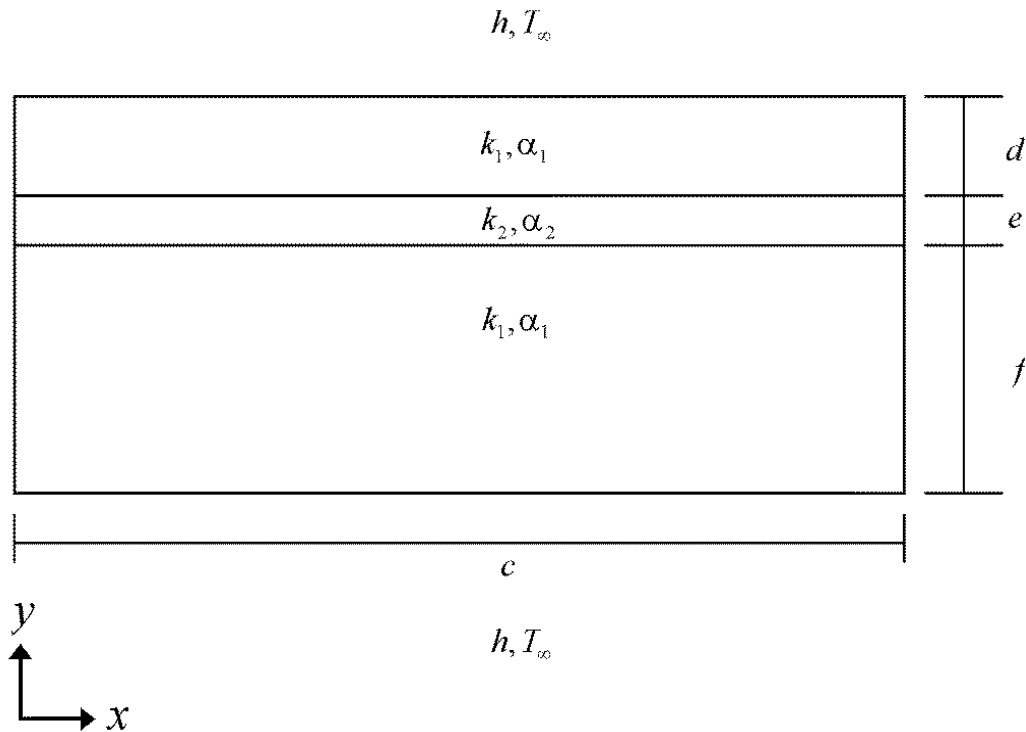


Figure 3.30: Overview of samples

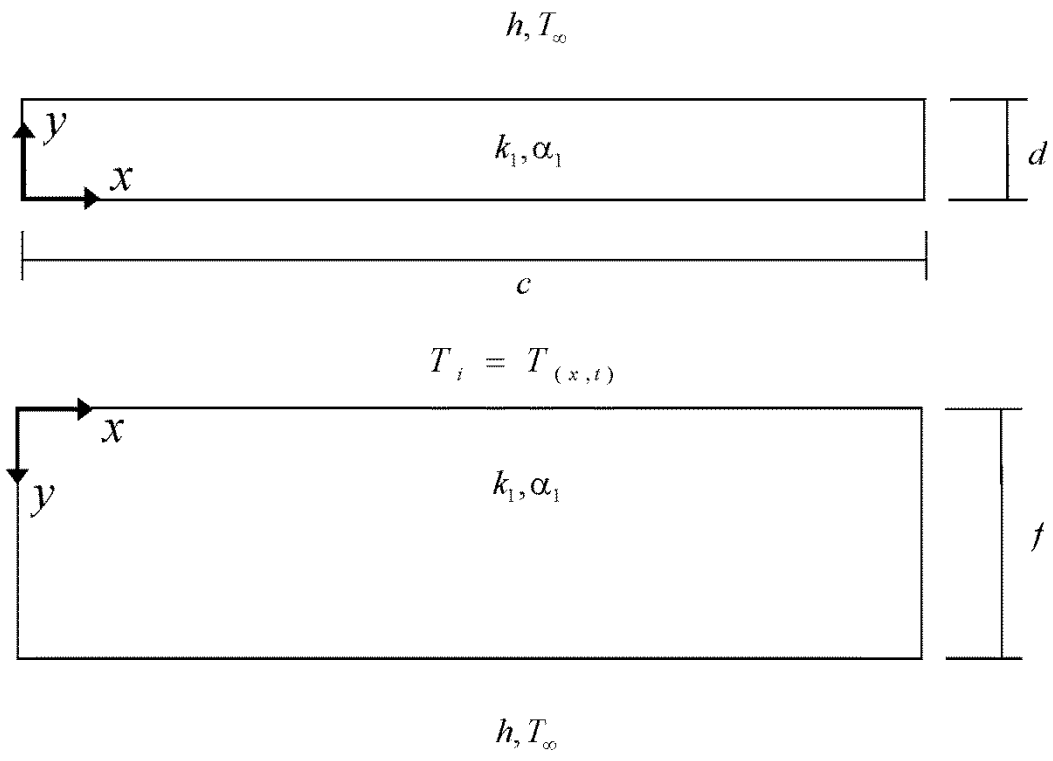


Figure 3.31: Boundary conditions of polymer samples

3.4.2 Heat Transfer Coefficient

The heat transfer coefficient model developed will be a general model applicable up to high Mach number flows in real applications. The heat transfer coefficient was determined based on an air velocity of 26.5 m/s from the second wind tunnel test (see Table 3.3). The air properties were taken at a film temperature of 42.6°C, based upon an average surface temperature of 61.3°C, and are shown in Table 3.4 [23].

$$T_{\text{fm}} = \frac{\bar{T}_i + T_\infty}{2} \quad (3.11)$$

Table 3.4: Air properties

Property	Value
Density	$\rho = 1.1182 \text{ kg/m}^3$
Dynamic viscosity	$\mu = 19.23 \times 10^{-6} \text{ kg/m} \cdot \text{s}$
Thermal conductivity (fluid)	$k_f = 0.02710 \text{ W/m} \cdot \text{°C}$
Specific heat capacity	$C_p = 1007.0 \text{ J/kg} \cdot \text{°C}$
Heat capacity ratio [5]	$\gamma = 1.4$
Prandtl number	$\text{Pr} = 0.710$

The Reynolds number characterizes the fluid flow regime over the flat plate. It is defined as the ratio of the fluid inertia stress to the viscous stress, and is calculated to be:

$$\text{Re}_L = \frac{\rho U_\infty L}{\mu} = \frac{1.1182 \frac{\text{kg}}{\text{m}^3} * 26.5 \frac{\text{m}}{\text{s}} * 0.1 \text{ m}}{19.23 \times 10^{-6} \frac{\text{kg}}{\text{m} * \text{s}}} = 1.54 \times 10^5 \quad (3.12)$$

Recall that the critical Reynolds number after which the flow is no longer laminar typically lies between 3×10^5 and 6×10^5 [2016]. Since this Reynolds number is less than the transitional Reynolds number for flow over a flat plate ($\text{Re}_{\text{tr}} = 3 \times 10^5$), the flow over the entire smooth polymer surface is expected to be laminar. However, when heat convection occurs along the coating surface, the flow is assumed to be turbulent since the rough surface would trip the flow [20, 24, 25]. The turbulent heat transfer coefficient will only be used in the numerical model section (see Section 3.4).

The Nusselt number, a non-dimensional form of the heat transfer coefficient, will be used to determine the heat transfer coefficient. The Nusselt number is defined as the product of the heat transfer coefficient and length of plate divided by the thermal conductivity of the fluid.

$$\text{Nu} = \frac{hL_c}{k_f} \quad (3.13)$$

It represents the ratio of heat transferred from a surface to the heat conducted away by the fluid, and is expected to be large due to the large air velocity [5]. Therefore, we expect the heat transfer to be convection dominated.

Laminar flow over flat plates can occur at high velocities over short lengths of the plates. Based on the conditions of the second wind tunnel test, the distance from the leading edge at which the flow becomes transitional (i.e., $Re_{cr} = 3 \times 10^5$) is 195 mm. Therefore, for laminar flow the local Nusselt number is calculated with Eq. 3.14a for Prandtl numbers between 0.6 and 10 [26]:

$$Nu_x = \frac{hx}{k_f} = 0.332(Re_x)^{1/2}(Pr)^{1/3} \quad (3.14a)$$

Integrating this result over the entire plate we obtain Eq. 3.14b:

$$\overline{Nu}_L = \frac{\bar{h}L}{k_f} = 0.664(Re_L)^{1/2}(Pr)^{1/3} = 232.7 \quad (3.14b)$$

For fluids flowing over a flat plate, with a Reynolds number between 2×10^4 and 3×10^7 , and a Prandtl number between 0.7 and 380, the average Nusselt number for turbulent flow is [27]:

$$\overline{Nu}_L = 0.037(Re_L)^{4/5}(Pr)^{0.43} \left(\frac{\mu_\infty}{\mu_0} \right)^{0.43} \quad (3.15a)$$

For air, the dependence of dynamic viscosity on temperature is very weak. Therefore, the dependence of the Nusselt number for turbulent flow on the ratio of the fluid free stream dynamic viscosity (μ_∞) to dynamic viscosity at the temperature of the wall (μ_0) is approximately 1 and can be ignored

$$\left(\frac{\mu_\infty}{\mu_0} \right)^{0.43} = \left(\frac{18.36 \times 10^{-6} \text{ kg/m} \cdot \text{s}}{20.09 \times 10^{-6} \text{ kg/m} \cdot \text{s}} \right)^{0.43} = (0.914)^{0.43} = 0.962 \quad (3.15b)$$

The Nusselt number for turbulent flow can be calculated as:

$$\overline{\text{Nu}}_L = 0.037(\text{Re}_L)^{4/5}(\text{Pr})^{0.43} = 451.3 \quad (3.15b)$$

The heat transfer coefficient for laminar flow is calculated to be:

$$\bar{h} = 0.664(\text{Re}_L)^{1/2}(\text{Pr})^{1/3} \frac{k_f}{L} = 63.1 \text{ W/m}^2 \cdot \text{°C} \quad (3.16)$$

For turbulent flow, it is:

$$\bar{h} = 0.037(\text{Re}_L)^{4/5}(\text{Pr})^{0.43} \frac{k_f}{L} = 122.3 \text{ W/m}^2 \cdot \text{°C} \quad (3.17)$$

As the air passes over the flat plate, the plate will be cooled by the air while being heated by fluid viscous shear work. The recovery factor, r , compensates for this fluid viscous shear work in the fluid by making use of the adiabatic-wall temperature, T_{aw} , which will be greater than the free stream temperature of the fluid [28].

$$T_{aw} = \left(1 + r \frac{\gamma - 1}{2} \text{Ma}^2\right) T_\infty \quad (3.18)$$

For laminar flows, experimental and theoretical analyses have shown that the recovery factor can be approximated over a large range of Prandtl numbers, velocities, and geometrical shapes [29] as

$$r = \sqrt{\text{Pr}} \quad (3.19)$$

In this case, the recovery factor for laminar flow will be taken as Eq. 3.25 since this is in good agreement with experimental data [28]. However, for turbulent flows the recovery factor will be taken as Eq. 3.26, also from experimental data up Mach numbers of 2.4 [28]:

$$r = \sqrt[3]{\text{Pr}} \quad (3.20)$$

Note that the Prandtl number is near unity for air, and as such, the laminar and turbulent recovery factors are also near unity.

In order to calculate the adiabatic wall temperature, we must determine the Mach number. The speed of sound in air (356.2 m/s) is calculated by assuming it is a perfect gas [30].

$$c = \sqrt{\gamma RT_{\text{fm}}} = \sqrt{1.4 \times 0.287 \text{ kJ/kg}^\circ\text{K} \times 315.75^\circ\text{K} \times \frac{1000 \text{ m}^2/\text{s}^3}{1 \text{ kJ/kg}}} \quad (3.21)$$

The Mach number is 0.07, which is subsonic.

$$\text{Ma} = \frac{U_\infty}{c} = \frac{26.5 \text{ m/s}}{356.2 \text{ m/s}} = 0.074 \quad (3.22)$$

3.4.3 Curve Fitting

From the steady-state spatial temperature results of the first and second wind tunnel experiments a relationship between the coating surface temperature and distance from the heating wire was obtained. Only the spatial temperature profile of the coating surface was curve-fitted since this is required for the analytical model, while the polymer surface temperatures are determined from the analytical model. Equation 3.23 shows the expected exponentially decaying temperature model, to which a natural logarithmic transformation was applied. This non-linear transformation simplified the model and normalized the residuals [31]. The transformation to linearize the results by taking the natural logarithm of both sides, after a substitution to compensate for the room temperature ($\hat{T}_i = T_i - C$), was made as shown in Eq. 3.23a [31, 32]:

$$T_i = Ae^{-Bx} + C \quad (3.23)$$

$$(T_i - C) = \hat{T}_i = Ae^{-Bx} \quad (3.23a)$$

$$\ln(\hat{T}_i) = -Bx + \ln(A) \quad (3.24)$$

The estimation of parameters of a nonlinear regression model can be carried out by similar methods as a linear regression model [33]. Therefore, the coefficient of determination, R^2 , was used to characterize the goodness of fit of the relationship. It should be noted that the coefficient of determination is a function of the experimentally measured temperature (T_e), average of the experimentally measured temperature (\bar{T}_e), and curve fit temperature (T_i) as shown in Eq. 3.25 [31]:

$$R^2 = 1 - \frac{SS_{\text{err}}}{SS_{\text{tot}}} = 1 - \frac{\sum_e (T_e - T_i)^2}{\sum_e (T_e - \bar{T}_e)^2} \quad (3.25)$$

Wind Tunnel – Test #1 with Coating Exposed

The coefficients A, B and C in Eq. 3.23 were obtained by maximizing the R^2 value.

$$A = 194.2, B = 91.2, C = 27.4, R^2 = 0.9992 = 99.92\% \quad (3.26)$$

The R^2 value obtained is above 99% indicating a good model fit. The accuracy of the trend line is also visible in Fig. 3.32 as shown below.

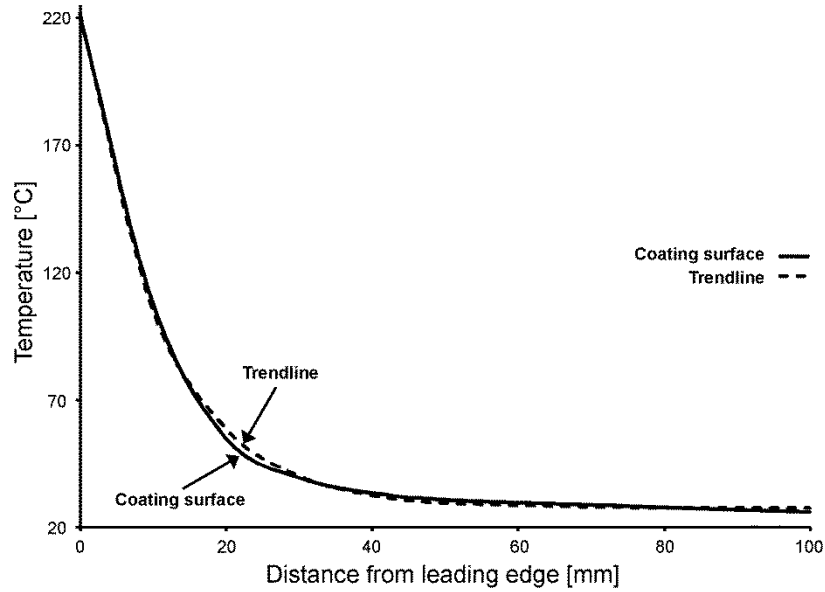


Figure 3.32: Spatial temperature profile of coating surface with expected trend line – 1st wind tunnel test with coating exposed

Although the exponentially decaying relationship obtained has a small error as evidenced by the coefficient of determination, the error is slightly greater at a distance 20 mm, and at distances greater than 40 mm from the heating wire. A relationship with an exponential with a second order polynomial was explored to reduce the error at large distance away from the heating wire, as shown in Eq. 3.27.

$$T_i = Ae^{(Bx^2+Cx)} + D \quad (3.27)$$

Once the parameters were optimized to reduce the coefficient of determination, shown in Eq. 3.25, this relationship still resulted in a large coefficient of determination, indicating a good overall fit as shown in Fig. 3.33. The coefficients obtained are shown in Eq. 3.28.

$$A = 197.2, B = 460.6, C = -96.1, D = 24.7 \quad (3.28)$$

$$R^2 = 0.9986 = 99.86\%$$

Since this second relationship did not result in a superior fit, as evidenced by the lower coefficient of determination, it will not be used in the analytical model.

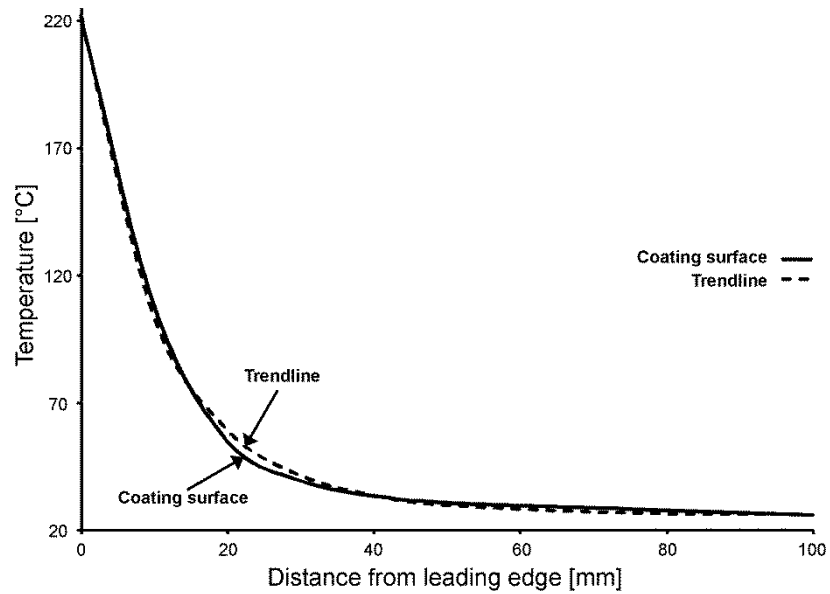


Figure 3.33: Spatial temperature profile of coating with alternative trend line
 – 1st wind tunnel test with coating exposed

Wind Tunnel – Test #2 with Top Polymer Layer

The temperature distribution of the coating surface from the second wind tunnel test was determined using a similar method. The coefficients from an exponentially decaying temperature relationship (see Eq. 3.23) are shown below in Eq. 3.29. The curve fit results are in good agreement with the experimental data as shown in Fig. 3.34:

$$A = 151.9, B = 121.1, C = 28.9 \quad (3.29)$$
$$R^2 = 0.9976 = 99.76\%$$

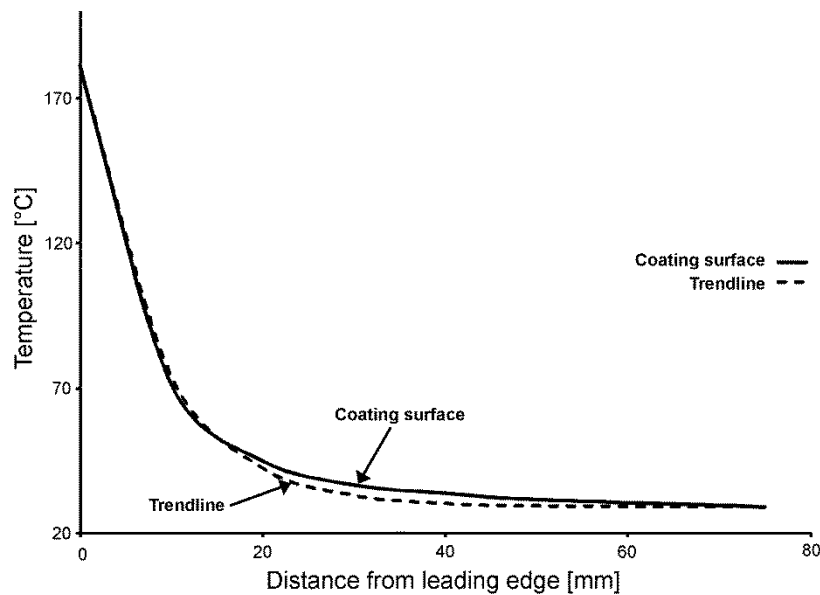


Figure 3.34: Spatial temperature profile of coating surface with expected trend line – 2nd wind tunnel test with top polymer layer

In this case, the error is noticeably greater at a distance more than 20 mm from the heating wire. Therefore, the decaying exponential with a second order polynomial temperature from the heating wire was also calculated (see Eq. 3.27). These results are shown in Fig. 3.35. The coefficients and coefficient of determination are shown below in Eq. 3.30:

$$A = 150.1, B = 460.5, C = -133.3, D = 31.1 \quad (3.30)$$

$$R^2 = 0.9994 = 99.94\%$$

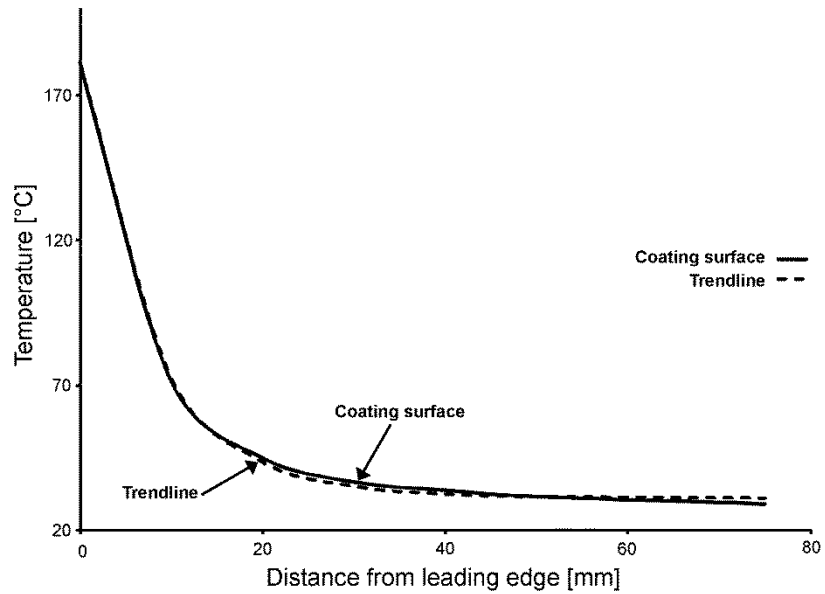


Figure 3.35: Spatial temperature profile of coating with alternative trend line
 – 2nd wind tunnel test with top polymer layer

For both wind tunnel tests, the best curve fit relationship, as evidenced by the coefficient of determination, will be used. For the second wind tunnel test, although the temperature is expected to decay exponentially from the heating wire, the exponentially decaying relationship will not be used since a slightly modified version has a better fit as indicated by the coefficient of determination.

3.4.4 Temperature Distribution

The analytical surface temperature distribution of the polymer surfaces of both wind tunnel tests can be determined from Eq. 3.10:

$$T_{(y)} = \frac{h(T_i - T_{aw})}{k + hd}y + T_{aw} \quad (3.10)$$

Recall from Table 2.2 that the top and bottom polymer thicknesses were 0.9 mm and 9.2mm, respectively. The laminar heat transfer coefficient was used since both polymer surfaces were smooth.

Wind Tunnel – Test #1 with coating exposed

The steady state results for both the analytical and experimental polymer surface temperature distribution of the first wind tunnel test are shown in Fig. 3.36.

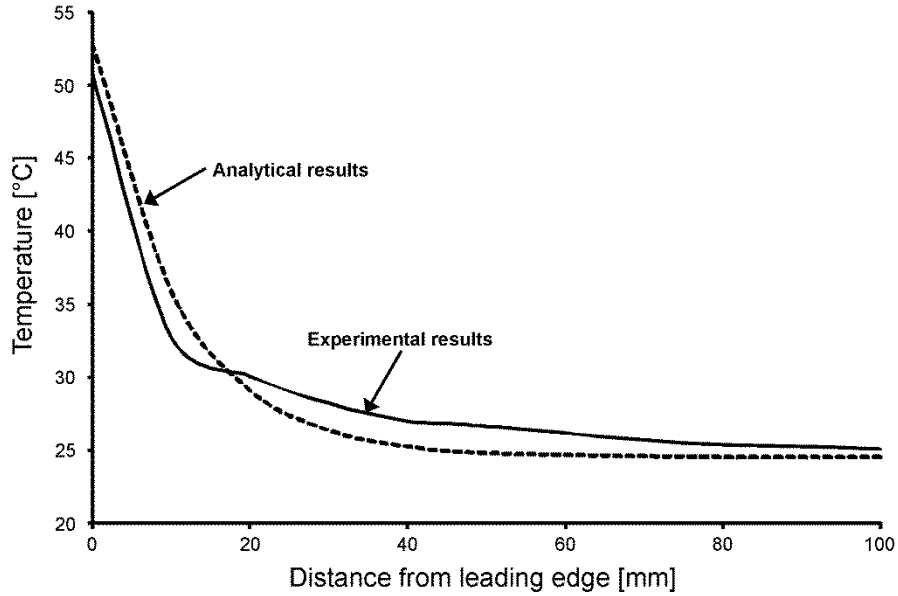


Figure 3.36: Experimental and analytical results of polymer surface – 1st wind tunnel test with coating exposed

Defining the error as Eq. 3.31:

$$\varepsilon = \text{abs} \left[\frac{T_e - T_{\text{analyt.}}}{T_e} \right] \times 100 \quad (3.31)$$

The greatest error between polymer experimental and analytical results is 9.5% at a distance of 10 mm from the heating wire. The average error from the heating wire to 100 mm thereafter is only 5.3%. Based on the relatively low error, the analytical results are in good agreement with the experimental results.

Wind Tunnel – Test #2 with top polymer layer

For the second wind tunnel test, both the top and bottom polymer surfaces were calculated analytically and are shown in Fig. 3.37.

At the heating wire along the bottom polymer surface, the temperature calculated by the analytical model is greater than the experimentally measured temperature by 24.8%. Past this point the experimental temperatures were all greater than the temperatures calculated analytically. This is evident since the second highest error is 8.4% at a distance 30 mm from the heating wire.

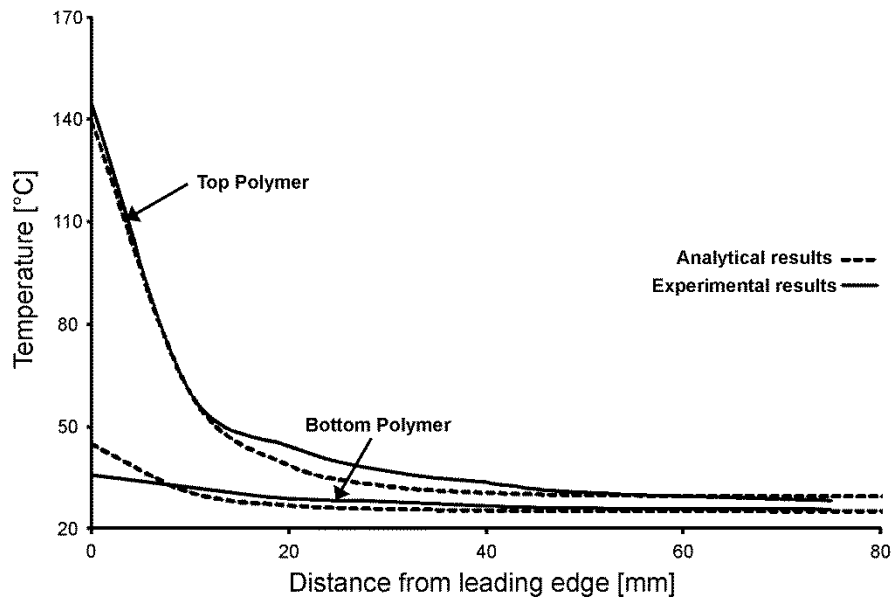


Figure 3.37: Experimental and analytical results of top and bottom polymer surfaces – 2nd wind tunnel test with top polymer layer

Along the top polymer surface, the greatest error is 12.6% at a distance of 20 mm from the heating wire while the average error is 6.2%. Both experimental and analytical temperatures converge around 50 mm from the heating wire.

The large error at the heating wire along the bottom polymer surface could be partially attributed to the 1-D heat conduction assumption in the analytical model. Since this model does not consider the conduction along the length of the samples, the analytical temperature will be higher near heating sources.

The bottom polymer's surface experimental temperature being lower than the analytical model's calculated temperature can be partially attributed to heat leaving the sample along the leading edge. This heat was seen in the airfoil along the leading edge, which was noticeably warmer than air temperature at the conclusion of the experiments. Although this may not be ideal, the aluminum airfoil can act a form of heat sink, preventing a much larger flux which could occur if this surface was exposed to the fast moving air. It should be noted that the airfoil would lose its heat to the air through convection as well, and thus there would still be a small flux along the samples' front face. At a distance 10 mm or greater, the analytical and experimental results are almost the same.

Away from this irregularity along the bottom polymer surface's leading edge, the analytical results are in good agreement with the experimental results.

3.5 Numerical Model

Numerical analysis was conducted to validate the experimental and analytical results of the first and second wind tunnel tests. The parameters used in the analytical and FEA models are summarized in Table 3.5. It should be noted that the heat transfer coefficient was laminar for all polymer surfaces, and turbulent for the coating surface due to flow tripping. Recall that the boundary conditions are detailed in the numerical method section of the experimental method (see Section 2.5). For both tests, the mesh was controlled to have fine elements over the coating surface, as well as near the leading edge of the polymer where the temperature gradient was large. Further, for the second wind tunnel test, the top polymer surface had a fine mesh applied to it since the temperature gradient was also expected to be large. Since both meshed geometries are similar, only the mesh of the second wind tunnel tests is shown in Fig. 3.38.

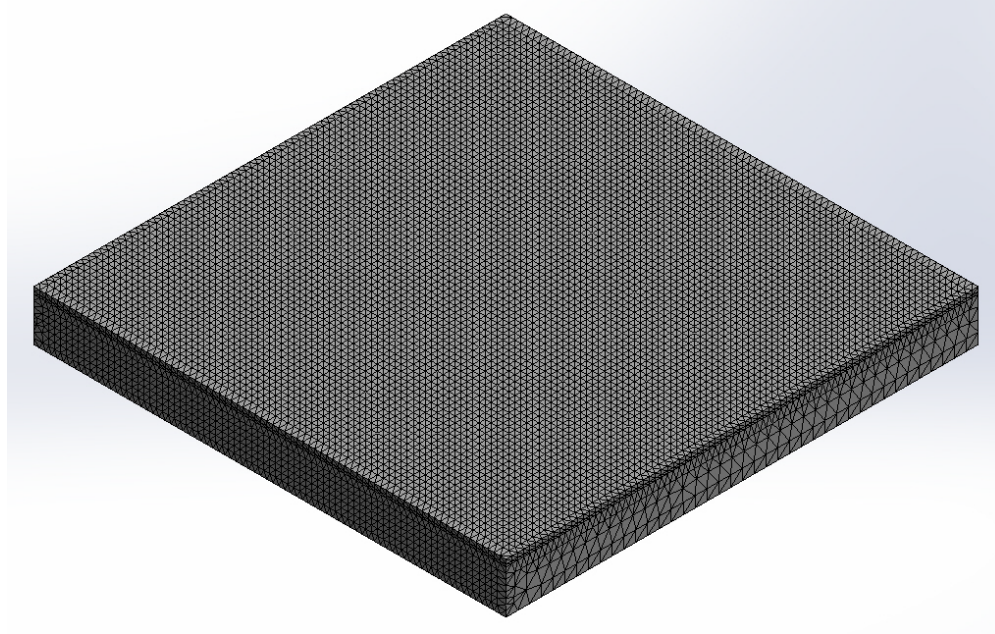


Figure 3.38: Mesh applied to geometry of second wind tunnel experiment

Table 3.5: Model parameters

Parameter	First Wind Tunnel Test	Second Wind Tunnel Test
Power	88.0 W	31.4 W
Wind speed	27.8 m/s	26.5 m/s
Heat transfer coefficient (laminar)	64.5 W/m ² °C	63.1 W/m ² °C
Heat transfer coefficient (turbulent)	127.1 W/m ² °C	N/A

3.5.2 Wind Tunnel – Test #1 with coating exposed

A cross-section of the numerical temperature results of the first wind tunnel test is shown in Fig. 3.39. Note that the turbulent heat transfer coefficient was used on the coating surface as part of the boundary condition. The temperature results predicted by the numerical model are shown in Fig. 3.40. The experimental temperature results are also included in order to make comparisons.

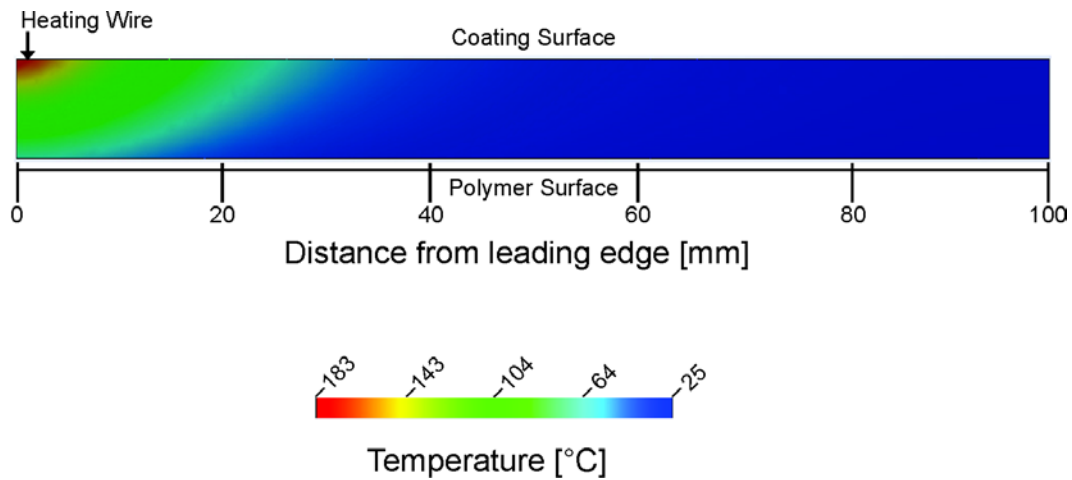


Figure 3.39: Numerical temperature results – 1st wind tunnel test with coating exposed

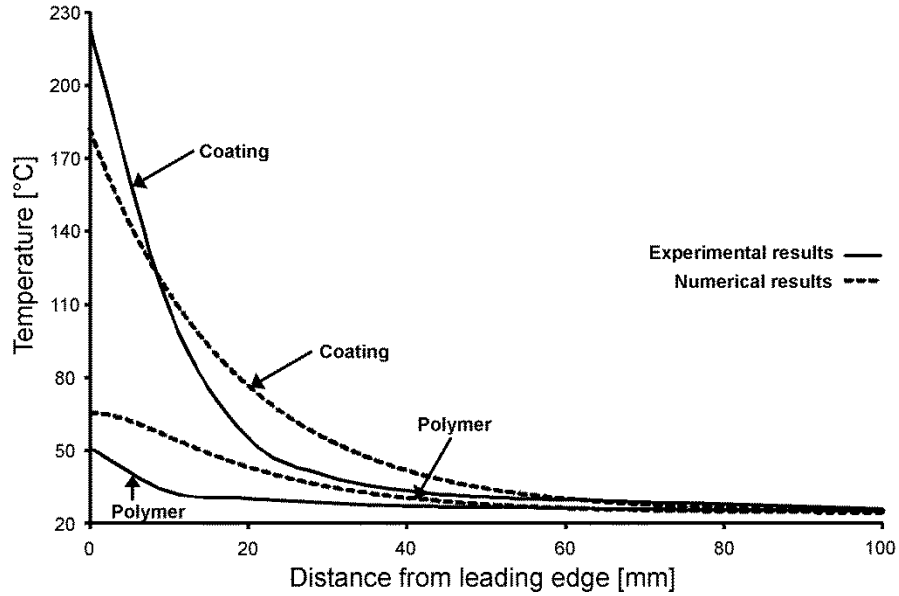


Figure 3.40: Experimental and Numerical Results – 1st wind tunnel test with coating exposed

There are noticeable differences in spatial temperatures between the numerical steady state results (see Fig. 3.40) compared to the experimental results after 6 minutes (see Fig. 3.25). Along the coating surface, the temperature calculated by the numerical model near the heating wire was 18% lower than the value that was experimentally measured. A potential explanation is the numerical model boundary condition assumption that half the energy is transferred to the sample and half to the air. If a greater portion of thermal energy enters the sample, then a higher temperature would be expected from the numerical model. Another potential explanation for this phenomenon is that the flow over the leading edge of the coating has not been fully tripped and therefore is not entirely turbulent. A lower heat transfer coefficient, resulting from a flow that is not entirely turbulent, would

reduce the total amount of heat removed from the coating surface, resulting in higher surface temperature during the experiment.

Beyond approximately 10 mm from the heating wire, the numerical model suggests that the coating is a more effective medium for heat conduction. The temperature calculated by the numerical was up to 21.7°C larger than the temperature experimentally measured. Away from the heating wire (50 mm), both the numerical and experimental results converge.

Along the polymer surface, the temperatures predicted by the numerical model are up to 22.5°C greater than those measured during the experiment. However again, beyond 50 mm from the heating wire, the temperatures converge. Near the heating wire (less than 20 mm), the increased polymer surface numerical temperature indicates that the numerical simulation shows more heat conduction through the polymer layer.

In both the analytical and numerical calculations, the polymer material properties are assumed to be isotropic as part of the ideal fiber-reinforced composites assumption. However, during the experiment, the polymer properties are anisotropic. Note that for this study, the polymer's transverse thermal conductivity is of most interest since we are examining the heat transfer through the samples. Wetherhold *et al.* [34] reported that while the longitudinal thermal conductivity can be predicted by a simple rule of mixtures, it is more problematic to predict the transverse thermal conductivity. The transverse thermal conductivity can be calculated using a combination of the parallel path and series conduction methods [35]. In this case, the parallel path method was used to calculate the isotropic thermal

conductivity, as detailed in Section 3.3.1, due to the microstructure of the polymer as shown in Fig. 3.2. It has been previously reported that the transverse conduction is roughly 5% less than the longitudinal conduction for a glass fiber fraction of 20% [35]. However, due to our glass fiber fraction of 38.3% (see Table 3.1), this anisotropic difference would be larger than 5% since there would be more conduction through the increased volume fraction of fiber. This anisotropic thermal conductivity contributes to surface temperature difference between the numerically calculated values and those measured during the experiments.

Transient Numerical Analysis – at Heating Wire

A transient numerical analysis of the first wind tunnel test sample was also performed. This was used to determine at which point in time the solution had approximately reached the steady state solution along both the coating and polymer surfaces at the heating wire. Recall that the experiment was performed for six minutes (See Figs. 3.18 and 3.19) and that steady state was achieved. The time steps were set to 60 seconds and solved for up to 20 minutes. The experimental results have been included with the transient results of the numerical model at the heating wire of both the polymer and coating surfaces and are shown Fig. 3.41.

The transient numerical analysis indicates that the polymer surfaces take roughly 25% more time to reach steady state than the coating surface. This same trend was observed during the experiments. Although the difference between the experimentally measured and numerically calculated temperatures are evident in Fig. 3.41, both the experimental and numerical results increase and decrease with similar trends. Therefore, the transient numerical analysis confirms that the steady state assumption is valid; further reinforcing that the experimental and analytical results are valid.

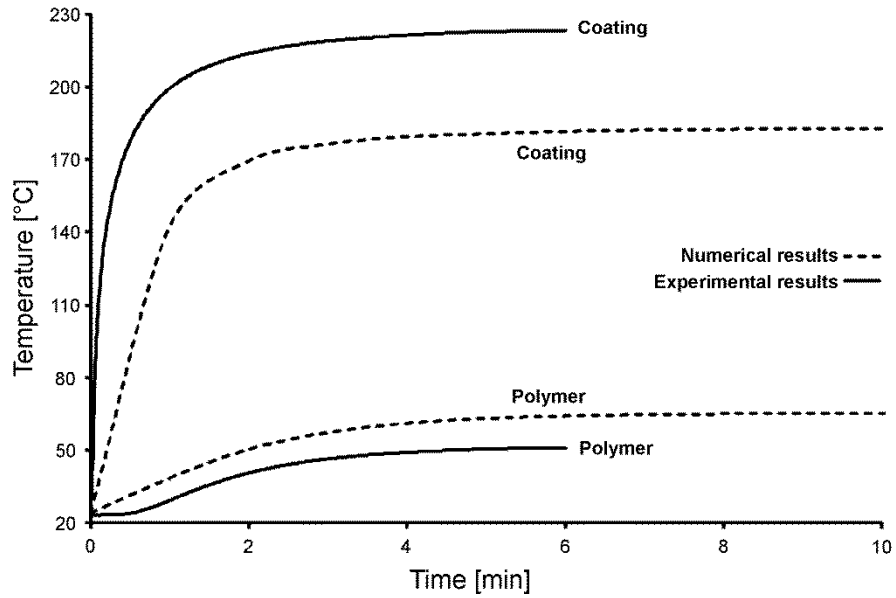


Figure 3.41: Numerical transient results – 1st wind tunnel test with coating exposed

3.5.3 Wind Tunnel – Test #2 with top polymer layer

A cross-section of the numerical temperature results of the second wind tunnel test is shown in Fig. 3.42. Both the experimental temperature and temperature predicted by the numerical model are included in Fig. 3.43 for the top and bottom polymer surfaces.

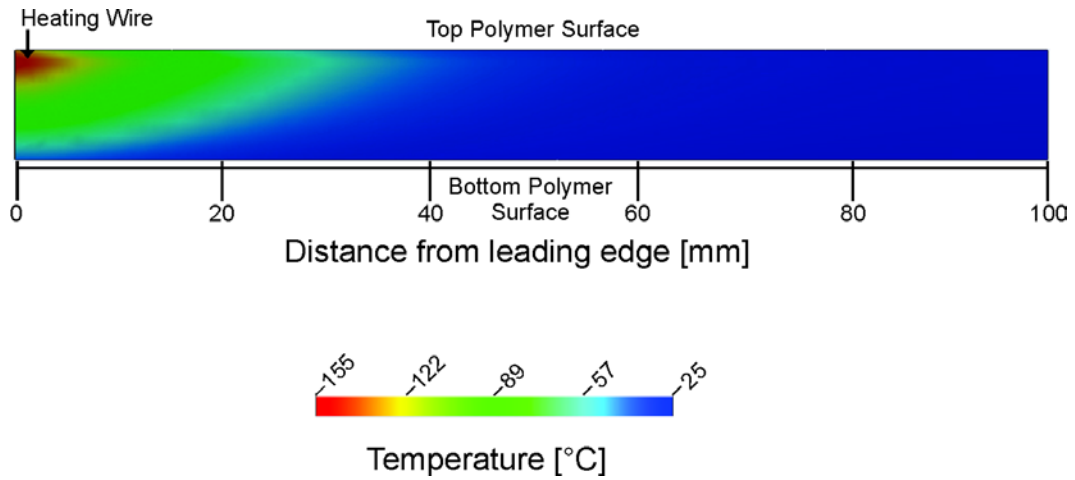


Figure 3.42: Numerical temperature results – 2nd wind tunnel test with top polymer layer

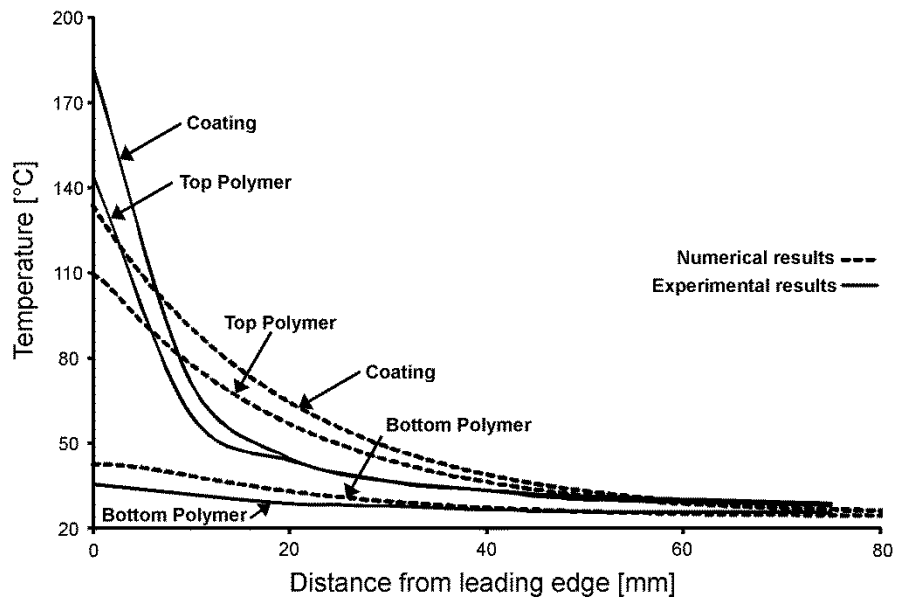


Figure 3.43: Numerical surface temperatures – 2nd wind tunnel test with top polymer layer

Although the heating wire is physically mounted between the coating and top polymer layers for 3 mm from the leading edge, there is no method to input this geometry into the numerical simulation. Instead the boundary condition used to input the heating power was along the leading face of the coating. Further numerical simulations, using the model of the first wind tunnel test were carried out with a heating power input along two different boundaries. Firstly, the heating power input was positioned over the first 3 mm of the top coating surface. This was possible since the coating surface was a physical boundary of the model and this boundary condition is identical to what is physically occurring. Secondly, the heating power input occurred at the sample's leading edge and only over the front face of the coating. Comparing the results of the two different sets of boundary conditions resulted in temperature less than 2% apart. The greatest deviation in the results obtained from experiment and numerical simulation was along the leading edge of the coating surface. At the leading edge, the actual boundary condition model calculated a temperature of 185.8°C, while the modified boundary condition model calculated a temperature of 182.5°C. For the second wind tunnel test, with the heating wire and coating embedded between the polymer layers, it is impossible to model a boundary condition between layers. However, since this introduced only a small error for the first wind tunnel test, the effects of the simplified boundary condition for the second wind tunnel test will be neglected.

From Fig. 3.43 of the second wind tunnel test, it is obvious that similar trends to Fig. 3.40 for the first wind tunnel test are occurring. At the

heating wire, both the coating and top polymer surface temperatures of the experiment are greater than the temperatures predicted by the numerical model by 26% and 24%, respectively. However, at a distance greater than 10mm, the temperatures calculated by the numerical model are higher by up to 20°C, with both results converging around 50 mm from the heating wire.

The numerical results of the bottom polymer surface were within 7°C of the experimental results. The numerical results from the second wind tunnel test were more similar than the results of the first wind tunnel test (See Fig. 3.40). This improvement could partially be attributed to the lower heating power. Again, all the temperatures, experimentally measured or numerical calculated, follow the same trends, decaying uniformly from the heating wire to a limited amount of heating 50 mm from the heating wire.

3.6 References

1. N. Huonnic, M. Abdelghnai, P. Mertiny, A. McDonald, Deposition and Characterization of Flame-Sprayed Aluminum on Cured Glass and Basalt Fiber-Reinforced Epoxy Tubes, *Surf. Coat. Technol.* 205 (2010) 867-873.
2. J. Melo, F. Neto, G. Barros, F. Mesquita, Mechanical behavior of GRP pressure pipes with addition of quartz sand filler, *J. Compos. Mater.* 45 (2010) 717-726.
3. A. McDonald, C. Moreau, S. Chandra, Use of Thermal Emission Signals to Characterize the Impact of Fully and Partially Molten Plasma-Sprayed Zirconia Particles on Glass Surfaces, *Surf. Coat. Technol.* 204 (2010) 2323-2330.
4. J. Taylor, *An Introduction to Error Analysis: the Study of Uncertainties in Physical Measurements*, University Science Books, Mill Valley, CA, 1982, pp. 89.
5. Y. Çengel, *Heat and Mass Transfer*, third ed., McGraw-Hill, Inc., New York, 2007, pp. 21, 236, 358, 842, 844-846.
6. C. . Katsoulis, B. Kandola, P. Myler, E. Kandare, Post-fire flexural performance of epoxy-nanocomposite matrix glass fibre composites containing conventional flame retardants, *Composites: Part A*, 23 (2012) 1389-1399.

7. A. Mouritz, S. Feih, E. Kandare, Z. Mathys, A. Gibson, P. Des Jardin, S. Case, B. Lattimer, Review of fire structural modelling of polymer composites, *Composites: Part A*, 40 (2009) 1800-1814.
8. L. Jiji, *Heat Conduction*, third ed., Springer, Inc., New York, 2009, pp. 36, 166.
9. M. Islam, A. Pramila, Thermal conductivity of fiber reinforced composites by the FEM, *J. Compos. Mater.* 33 (1999) 1699-1715.
10. L.E. Evseeva, S.A. Tanaeva, Thermal Conductivity of Micro- and Nanostructural Epoxy Composites at Low Temperatures, *Mech. Compos. Mater.* 44 (2008) 87-92.
11. K.I. Horai, G. Simmons, H. Kanamori, D. Wones, Thermal diffusivity and conductivity of lunar material, *Sci.* 167 (1970) 730-31.
12. A. Patnaik, P. Kumar, S. Biswas, M. Kumar, Investigations on micro-mechanical and thermal characteristics of glass fiber reinforced epoxy based binary composite structure using finite element method, *Comput. Mater. Sci.* 63 (2012) 142-151.
13. S. Black, Flying high on composite wings, *High-Perform. Compos.* 16 (2008) 62-69.
14. S. F. Madsen, J. Holboell, M. Henriksen, F.M. Larsen, L.B Hansen, K. Bertelsen, Breakdown tests of glass fibre reinforced polymers (GFRP) as part of improved lightning protection of wind turbine blades, 2004 IEEE International Symposium on Electrical Insulation, Indianapolis, USA, September 19-22, 2004, Institute of Electrical and Electronics Engineers, 2004, pp.484-491.

15. G. Lubin, Handbook of Composites, Van Nostrand Reinhold, New York, 1982, pp. 745.
16. F. Gil, Learning from aircraft fuel tank explosions, Loss Prevention Bulletin. 203 (2008) 3-18.
17. X. Hui, K. Kumar, C. Sung, T. Edwards, D. Gardner, Experimental studies on the combustion characteristics of alternative jet fuels, Fuel, 98 (2012) 176-182.
18. "Standard test method for autoignition temperature of liquid chemicals", E659, 2005, Annual Book of ASTM Standards, ASTM, 2005.
19. D. Drysdale, An introduction to fire dynamics, third ed., John Wiley & Sons, Ltd., West Sussex, UK, 2011, pp. 246.
20. G. Nellis, S. Klein, Heat Transfer, Cambridge University Press, Ltd., New York, 2009, pp. 399, 510, 607, 691.
21. E. Eckert, Survey on heat transfer at high speeds, United States Air Force, 1961, pp. 50.
22. J. Kaye, The Transient Temperature Distribution in a Wing Flying at Supersonic Speeds, M.I.T. Division of Industrial Cooperation, 1949, pp. I, 34.
23. P. Oosthuizen, D. Naylor, An Introduction to Convective Heat Transfer Analysis McGraw-Hill, Inc., New York, 1999, pp. 66, 607.
24. E. Bardal, P. Molde, T. Eggen, Arc and Flame-Sprayed Aluminum and Zinc Coatings on Mild Steel: Bond Strength, Surface Roughness, Structure and Hardness, Br. Corros. J., 8 (1973) 15-19.

25. R. Starosta, Properties of Thermal Spraying Ni-Al Alloy Coatings, *Adv. Mater. Sci.*, 9 (2009) 30-40.
26. H. Schlichting, *Boundary-Layer Theory*, seventh ed., McGraw-Hill, Inc., New York, 1979, pp. 298.
27. A. Zhukauskas, A. Ambrazyavichyus, Heat transfer of a plate in a liquid flow, *Int. J. Heat Mass Transfer*, 3 (1961) 305-309.
28. A. Shapiro, *The Dynamics and Thermodynamics of Compressible Fluid Flow*, 2 vols., Ronald Press Co., New York, 1953, pp. 211-212, 1071, 1123.
29. J. Kaye, Survey of Friction Coefficients, Recovery Factors, and Heat Transfer Coefficients for Supersonic Flow, *J. Aeronaut Sci.*, 21 (1954) 117-129.
30. P. Kundu, I Cohen, *Fluid Mechanics*, fourth ed., Academic Press, Inc., Oxford, UK, 2008, pp. 719.
31. Cohen: J. Cohen, P. Cohen, S. West, L. Aiken, *Applied Multiple Regression/Correlation Analysis for the Behavioral Sciences*, third ed., Lawrence Erlbaum Associates, Inc., New Jersey, 2003, pp. 221, 229-231, 248.
32. R. Bethea, B. Duran, T. Boullion, *Statistical Methods for Engineers and Scientists*, Marcel Dekker, Inc., New York, 1975, pp. 307.
33. J. Neter, M. Kutner, C. Nachtsheim, W. Wasserman, *Applied Linear Statistical Models*, fourth ed., Irwin, Inc., Chicago, 1996, pp. 535.
34. R. Wetherhold, J. Wang, Difficulties in the Theories for Predicting Transverse Thermal Conductivity of Continuous Fiber Composites, *J. Comp. Mater.*, 28 (1994) 1491-1498.

35. G. Kalaprasad, P. Pradeep, G. Mathew, C. Pavithran, S. Thomas, Thermal conductivity and thermal diffusivity analyses of low-density polyethylene composites reinforced with sisal, glass and intimately mixed sisal/glass fibres, *Comp. Sci. Technol.*, 60 (2000) 2967-2977.

Chapter 4 Conclusions

Flame-sprayed metallic coatings were successfully deposited on GFRP substrates without causing apparent fiber damage. The heat transfer of the composite structures was examined with the boundaries insulated and under forced convection cooling. The results indicate that the composite structure is effective at conducting heat. The composite structure noticeably increased the surface temperature up to 50 mm from the heating source, thereby also reducing the temperature at the heating source.

The first phase of this study focused on the deposition and characterization of a metallic coating on a GFRP substrate. From SEM images it was determined that there was no fiber damage following flame spraying, if a layer of garnet sand was embedded in an epoxy matrix during polymer curing. The coating was characterized using EDX as well as XRD to determine the composition and that no oxides were formed.

The second phase of this study examined the heat transfer of the coating-polymer structure. In the preliminary insulated tests in Section 3.2.1 it was determined that the coating is effective at conducting heat throughout the coating-polymer ensemble. This concept was refined to include thicker polymer samples with the first wind tunnel tests. This experiment determined that thick polymer samples experience a significant temperature drop while the coating effectively conducts the heat along the top surface. Finally a similar method was applied in the second wind tunnel tests to

protect the coating from the ambient fluid, while also applying our knowledge from both previous experiments.

The third and final phase of this project examined analytical and numerical modelling of the structure's heat transfer. This phase included deriving a heat transfer coefficient applicable over a wide range of air speeds such that the model was as general as possible. The steady state experimental results were curve fit to obtain a relationship between the location from the heating wire and temperature along the coating surface. The numerical model was used to validate some of the assumptions in the analytical model.

From this study, it has been determined that the concept of using a metal on a polymer to conduct heat is practical and effective. Although this concept is being used in a proprietary manner commercially, there is limited scientific literature available [1]. As polymers become more widely used in industry, the applications for this concept will increase. Therefore, this study aims to contribute in this area and further future work for similar applications.

4.1 Future Work

The focus of this study was to quantify the heat transfer performance of a metallic coating on a polymer flat plate. A similar concept is being used to de-ice concrete runways, with a conductive concrete powered by photovoltaic cells to heat the surface. This has made the “runways safer and less expensive to maintain during winter months” [2]. Polymers are already used in many concrete structures due to corrosion resistance, non-magnetic properties, high tensile strength and light weight [3]. However, there are cost and temperature restrictions to their applications [3]. By extension, coupling the work from this study for polymers with alternatives power sources for stationary applications could be investigated. Currently, the only method of stationary de-icing not requiring spraying a fluid being utilized is infra-red heating [4]. Connecting the heating elements from a coating-polymer system could achieve a more uniform surface temperature distribution across the airfoils. This more uniform temperature distribution would reduce hot spots and ensure that the temperature of the polymer is below the glass transition temperature. The resin system glass transition temperature is lower than that of the glass fibers and, therefore, will be the limiting factor. Above the glass transition temperature there is significant drop in Young’s modulus, which will reduce structural integrity of the polymer [5]. Combining this system with an external power source to provide more power than is available in-flight could reduce the de-icing time while presenting another alternative stationary de-icing system not requiring fluid to be sprayed.

Further, due to the increased thermal mass of polymer airfoils over metallic airfoils, the heating effects of the stationary de-icing process would be present for longer.

Other applications that could be pursued further involve polymer pipes. A composite coating-polymer heating system could potentially eliminate the need for heat tracing. Further, this heating system could be coupled with a structural health monitoring system to ensure the integrity of the pipe.

Alternative metallic coatings could be further investigated. Using a coating with a much higher electrical resistance could eliminate the need for a heating wire, since the electrical current would flow through the coating and produce uniform temperature at the coating surface. As preliminary experimental tests have shown, melting a nickel-chromium (80 wt. % nickel-20 wt. % chromium, Ni-20Cr) powder currently requires slightly more heat than the polymer substrates can tolerate; therefore, exploring high temperature polymers with coating systems could provide promising results.

4.2 References

1. J. Sloan, 787 integrates new composite wind de-icing system, *High Performance Composites*, 2009, 17(1), pp. 27-29.
2. Anti-icing runway uses conductive concrete slabs, *Advanced Materials & Processes*, 2012, 170(1) pp. 4.
3. A. Naaman, FRP Reinforcements in Structural Concrete: Assessment, Progress, and Prospectus, Proceedings of the Sixth International Symposium on FRP Reinforcement for Concrete Structures (FRPRCS-6), Singapore, July 8-10, 2003, World Scientific Publishing Co., pp. 3-24
4. Preliminary data summary: airport deicing operations (revised), 2000, Washington, DC: US Environmental Protection Agency, Office of Water, pp. 6-11 to 6-16.
5. E. Chowdhury, R. Eedson, M. Green, L. Bisby, N. Benichou, Mechanical Characterization of Fibre Reinforced Polymers Materials at High Temperature, *Fire Technology*, 2011, 47, pp. 1063-1080.

Appendix

4.3 Appendix 1

4.3.1 MATLAB Code:

```
function [] = DTJuly25

clear all, close all

format long e;

%k1 = 237;
%a1 = k1/(0.9*(2.7*1000*1000));

k1 = 0.88;           %W/mK thermal conductivity

c = 0.1;             %m      length in x
d = 0.0092;         %m      thickness in y
h = 63.1;           %W/m^2K
T_inf = 24.01;      %temperature of fluid for convection

Nx = 51;             %number of x values
Ny = 11;             %number of x values
incX = (c-0)/(Nx-1);
incY = (d-0)/(Ny-1);

xad = 0:incX:c;
yad = 0:incY:d;
x_cord = zeros(1,length(xad));
y_cord = zeros(1,length(yad));

for x = 1:length(xad)
    x_cord(1,x) = xad(1,x);
end

for y = 1:length(yad)
    y_cord(1,y) = yad(1,y);
end

ac = 151.1;
bc = -121.1;
cc = 28.9;

T = zeros(1,length(xad));
```

```

for x = 1:length(xad)
    T(1,x) = ac*exp(x_cord(1,x)*bc)+cc;
end

SolutionXY = zeros(length(xad),length(yad));

for y = 1:length(yad)
    for x = 1:length(xad)
        SolutionXY(x,y) = SolutionXY(x,y) + (T_inf-
T(1,x))/(k1/h+d)*y_cord(1,y)+T(1,x);
    end
end

disp('break')

F = zeros(length(xad),2);

for x =1:length(xad)
    n = max(y);
    F(x,1) = SolutionXY(x,1);
    F(x,2) = SolutionXY(x,n);
end

figure(1)
v = [0 c T_inf (T_inf+170)];
plot(xad,F),axis(v)
title('Temperature profile at Steady State')
grid, xlabel('Distance [x] (m)'), ylabel('Tempearture (C)')
legend('at coating','at top')

end

```